Large-Eddy Simulation of an Axisymmetric Shock-Wave/Boundary-Layer Interaction at Mach 2.5

Layton W. Howerton*, Gregory A. Blaisdell†, and Jonathan Poggie‡
Purdue University, West Lafayette, Indiana 47907

Implicit large-eddy simulation (ILES) of a turbulent, axisymmetric, shock-wave/boundary-layer interaction was performed at Mach 2.5. The simulation was performed to compare to recent experimental work completed at NASA Glenn Research Center (GRC) under the Turbulent Computational Fluid Dynamics Validation Experiment (TCFDVE). The circular test section of the TCFDVE allows shock-wave/boundary-layer interactions to be studied without corner effects. The ILES was completed using a low-dissipation, hybrid advection scheme available in VULCAN-CFD which blends a fourth-order symmetric reconstruction with a third-order upwind-biased MUSCL scheme. The method of recycling/rescaling was used to generate a scale-resolved turbulent boundary layer. To save on computational cost, a Reynolds-averaged Navier-Stokes (RANS) solution was imposed at some boundary conditions. Comparison to experimental data showed promising results. PIV, Pitot, wall static pressure taps, and hot-wire data were used for comparison. With significant computational resource allocation, the current two billion point ILES simulation was run at an experimental Reynolds number for approximately 102 cycles of the dominant low-frequency breathing motion of the separation bubble created by the shock-wave/boundary-layer interaction.

Nomenclature

C_f	=	skin friction coefficient
D	=	Test section diameter
f_s	=	Sampling frequency
$G(f)$	=	power spectral density
M	=	Mach number
P	=	Pressure
r	=	Radial coordinate
Re	=	Reynolds number
St	=	Strouhal number
T	=	Temperature
t	=	Time
u_τ	=	Friction velocity
V	=	Velocity vector
x	=	Streamwise coordinate
$\Delta(x, y, z)^+$	=	Nondimensional coordinates in viscous wall units
δ	=	Boundary layer thickness
δ^*	=	Boundary layer displacement thickness
θ	=	Boundary layer momentum thickness; azimuthal coordinate
ν	=	Kinematic viscosity
ρ	=	Density

*Graduate Student, School of Aeronautics and Astronautics, AIAA Student Member.
†Professor, School of Aeronautics and Astronautics, AIAA Associate Fellow.
‡Professor, School of Aeronautics and Astronautics, AIAA Associate Fellow.

Subscript

$_D$ = Test section diameter reference
$_i$ = Inviscid shock impingement
$_t$ = Stagnation
$_w$ = Wall
$_1$ = Incoming station
$_\infty$ = Freestream

I. Introduction

Settles and Dodson [1] worked to compile a database of experimental data for supersonic and hypersonic flows. In their compilation, an effort was made to categorize the particular dataset as a good candidate to be a computational validation experiment. Validation of computational models is critical for the community to improve the models that drive design cycles. Many factors can limit a given experimental dataset's utility as a computational validation case. One of these factors may be assuming a flow is nominally 2D on the centerline of a wind tunnel with a rectangular cross section where the three-dimensionality of the corners contaminates the centerline behavior. Another example could be an under-defined upstream flow, the details of which are required for computational upstream boundary conditions. Corroborating independent measurement techniques are also important for validation to drive down uncertainties in the experimental dataset. Settles and Dodson found that most of the experiments collected in their dataset were not appropriate for CFD validation. To a similar end, a workshop was held at the 48$^{\text{th}}$ AIAA Aerospace Sciences Meeting to discuss the accuracy of computationally simulating nominally 2D shock-wave/boundary-layer interactions (SWBLI) [2]. The workshop concluded there was a need for experimental datasets designed with CFD compatibility in mind which did not include sidewall effects. In a review by Gaitonde and Adler [3], several examples are presented where the presence or absence of sidewalls changes the unsteady 3D flow dynamics. Poggie and Porter [4] found significant differences in compression corner SWBLI unsteadiness when comparing solutions with periodic versus sidewall boundary conditions at Mach number 2.25. Vyas [5] studied the discrepancies that arise from the often used computational assumption that the flow is nominally 2D on the centerline when simulating wind tunnels with rectangular cross-sections. Vyas simulated 2D, 3D periodic, and 3D half-span rectangular wind tunnels including a shock-wave/boundary-layer interaction using a Reynolds-averaged Navier-Stokes (RANS) solver then 3D periodic and 3D full-span wall-resolved large-eddy simulation (LES) of the same flow. Simulations including corner effects as opposed to periodic boundary conditions changed the interaction length scale of the shock-wave/boundary-layer interaction and had increased three-dimensionality. Simulating a configuration without corner effects presents an opportunity to trade some computational cost which would be incurred with a full-span domain size for increased resolution. More confidence can be given to a periodic boundary condition when the physical geometry being represented is axisymmetric. A flow without corner effects also could reduce the uncertainty as to if achieved computational error relative to experimental data is due to fundamental CFD modeling choices as opposed to missing key three-dimensionality caused by corners.

Shock-wave/boundary-layer interactions are one category of flow which lower computational cost methods tend to struggle to predict correctly. RANS solvers have difficulty with shock-wave/boundary-layer interactions in part due to many common turbulence models being tuned to equilibrium turbulence. The unsteadiness of SWBLI also motivates the use of time-accurate methods. The unsteady nature of SWBLI is a very active area of research [6]. The work of the Turbulent Computational Fluid Dynamics Validation Experiment (TCFDVE) at NASA Glenn Research Center (GRC) was initiated to provide a high-quality experimental dataset with these considerations in mind. The TCFDVE was a multi-year test campaign designed to address the difficulties associated with creating a CFD validation test case on a known problem area for RANS methods. The circular test section of the tunnel removed the often uncharacterized 3D effects. In a extension of the TCFDVE dataset, asymmetric tests were also done in which swept 3D shocks are formed by offsetting the shock generator (SG) from the tunnel centerline. For the present work, only the axisymmetric case is considered. Several independent experimental techniques were used in the TCFDVE including: PIV, Pitot probe, wall static pressure taps, and hot-wire surveys. The data collection includes data far upstream of the interaction, useful for computational inflow boundary conditions.

The simulations presented here represent just one portion of the overall work completed to date surrounding the TCFDVE. Computational work in Refs. [7–10] has laid the groundwork for the presented work. Unlike previous the work of Mosele et al. [7–9], the Reynolds number of the ILES is not lowered below the experimental values for

computational cost considerations. The precursor RANS simulation, which was used to create implicit large-eddy simulation (ILES) boundary conditions, was an extension of the effort at NASA GRC to create a new validation case for the NASA Turbulence Modeling Resource (TMR) [10]. The RANS computational grid used in this work is the same grid which will be provided in the NASA TMR validation case. The experimental data in Refs. [11–16] are used to ground the computations presented here to experimental methods. This work is the authors' first of several planned and in-progress high-fidelity simulations of the TCFDVE as well as the follow on High-Mach Validation Experiments (HMVE) in the same facility.

II. Methodology

The structured computational mesh was created with the Pointwise grid generation software [17]. Post-processing of the computational solution was completed with Tecplot [18] and MATLAB software [19]. VULCAN-CFD is a Navier-Stokes flow solver maintained by NASA Langley Research Center. VULCAN-CFD is capable of using unstructured and structured computational grids and can complete RANS simulations, hybrid RANS/LES, and large-eddy simulations [20, 21]. Only the structured grid solver is used in the present work.

A. Geometry and Freestream Conditions

The boundary layer portion of the shock-wave/boundary-layer interaction being studied here is the naturally occurring boundary layer on the circular test section wall of the NASA GRC 225 cm^2 Wind Tunnel, seen in Fig. 1. The shock is produced by a cantilevered, axisymmetric cone-cylinder located on the tunnel centerline. A view of an example cone-cylinder in the tunnel can be see in Fig. 2 from Ref. [11]. The axisymmetric shock from the leading edge of the cone-cylinder, as well as the expansion fan over the shoulder of the cone-cylinder, impinge on the test section boundary layer and create a shock-wave/boundary-layer interaction. The converging-diverging nozzle used in the TCFDVE creates nominally Mach number 2.5 flow in the test section. The facility inlet air heater was used to control the total temperature to 310.9 K (100 °F). The tunnel is a continuous flow facility, and using the temperature control abilities, the walls are considered adiabatic. The shock-generator cone half-angle is 16 degrees, and the cylindrical portion of the shock-generator has a diameter of 5 centimeters. The tunnel test section diameter, D, is 17 centimeters. Often in the experimental data, the Reynolds number is presented based on test section diameter. The NASA TMR effort was conducted at a $\mathrm{Re}_D = 4E6$ where most of the original data were collected. In working with the experimental group at NASA GRC, lower Reynolds number runs were completed to attempt to overlap with the computational limitations of high Reynolds number implicit LES. However, at the lower Reynolds numbers, the probe-based measurement techniques would contaminate the SWBLI or unstart the tunnel due to downstream blockage. Thus in this work, direct comparison will be done to PIV, but probe data will be at a higher Reynolds number. Current work is being done to run ILES cases at conditions at which all experimental data are available at the same tunnel conditions. As informed by private communication with the experimental group at NASA GRC, the LES boundary conditions were created from *a priori* best estimates for conditions at the lower Reynolds number, $\mathrm{Re}_D = 1E6$, at which the present work focuses. The documentation for the lower Reynolds number tests was recently published in Ref. [16]. Additional details of the experimental facility can be found in Ref. [14]. The freestream conditions are listed in Table 1.

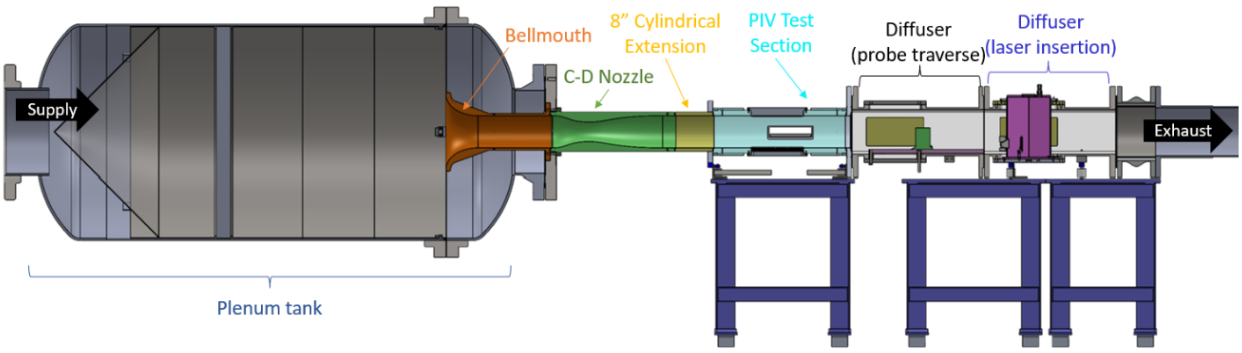

Fig. 1 NASA GRC 225 cm^2 Wind Tunnel, public domain, US government work [14].

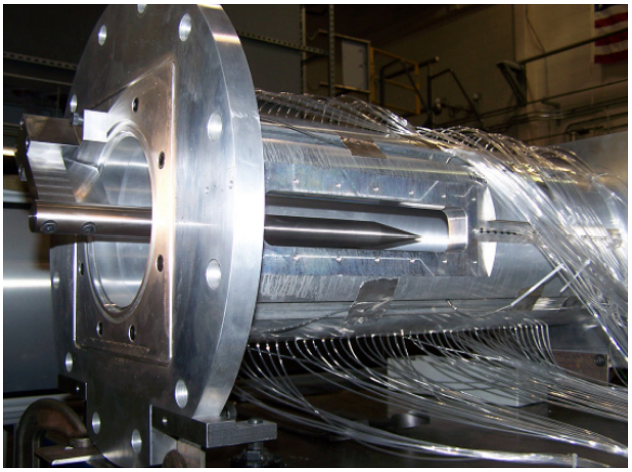

Fig. 2 NASA GRC 225 cm^2 Wind Tunnel with a cone-cylinder shock generator, public domain, US government work [11].

Table 1 Freestream flow conditions.

Parameter	Value
M_∞	2.49
ρ_∞	0.0956 kg/m^3
P_∞	3810 Pa
T_∞	139 K
$V_{x,\infty}$	588 m/s
$P_{t,\infty}$	6.41×10^4 Pa
$T_{t,\infty}$	311 K
Re_∞	5.88×10^6 m^{-1}
$\mathrm{Re}_{\theta,1} = \frac{\overline{u_\infty}\theta}{\nu_w}$	3160

B. Precursor RANS

To create proper inflow boundary conditions for the ILES domain, a precursor RANS case was calculated. Aside from the lower Reynolds number of $\mathrm{Re}_D = 1E6$, the presented RANS mirrors the work presented by Friedlander et al. [10]. The first author of this paper completed the VULCAN-CFD simulations in the NASA TMR work in Friedlander et al. [10]. The details of the simulation will be discussed then the data extracted for ILES boundary conditions will be explained.

By simulating the entire tunnel from upstream of the converging-diverging nozzle, the intention was to create an inflow turbulent boundary layer to the SWBLI that was as realistic as possible. The computational domain was 2D axisymmetric. Figure 3 shows the 2D solution with a 270° gray solid body rotation of the computational tunnel wall to better illustrate the geometry. The RANS grid did not model the upstream plenum or bellmouth inlet seen in Fig. 1, but included a length of constant area upstream of the converging-diverging nozzle. The computational grid has $5.56E5$ points, with a nominal wall spacing of $y^+ = 0.34$. For additional grid details, including grid convergence as part of the NASA TMR validation case development see Ref. [10]. The inflow was a subsonic boundary condition using tunnel total pressure and total temperature values provided by the experimental group at NASA GRC and listed in Table 1. The walls were modeled as adiabatic. The outflow was a 1^{st}-order extrapolation. The tunnel centerline was an axisymmetric axis boundary condition. The Spalart-Allmaras (SA) turbulence model was used [22]. The RANS simulations used the LDFSS flux construction [23] with the min-mod flux limiter.

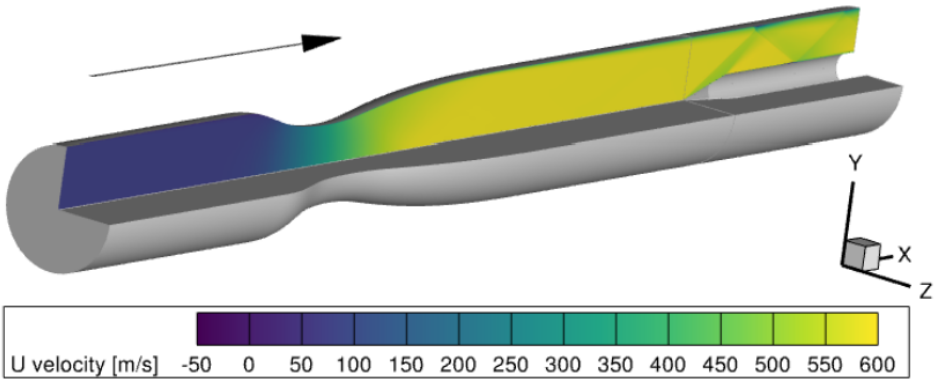

Fig. 3 VULCAN-CFD axisymmetric RANS solution with cutaway computational tunnel and SG visual aid.

The primary purpose of the RANS calculation was to provide mean boundary condition information for ILES. Due to the *a priori* nature of the case, the targeted versus achieved boundary layer quantities were not tuned to the experimental data prior to their use as ILES boundary conditions. The time and computational cost associated with ILES did not allow for the authors to wait until the experimental data collection at the current Reynolds number to take place. The location upstream of the interaction at which the RANS data was sampled for the boundary condition data was dictated by the recycling/rescaling method used to generate turbulent eddies in the ILES. As this work focuses on the ILES, an x coordinate zeroed at this station and nondimensionalized by the test section diameter is used throughout, $x/D = 0$. Figure 4 shows a portion of the RANS domain in this coordinate system. Additional details about the recycling/rescaling setup are found in Section II.D. The furthest upstream station for the experimental data presented in [16] is at $x/D = 1.288$. The boundary layer parameters for the RANS, ILES, and experimental data at $x/D = 1.288$ are shown in Table 2. Given the *a priori* nature of the computation and therefore the inability to adjust the RANS solution to experimental data prior to its use as the ILES boundary conditions, the errors are deemed acceptable. The momentum and displacement thicknesses are calculated accounting for the concavity of the tunnel wall; see Ref. [10]. The similarity between the RANS and ILES boundary layer properties serves as a validation that the recycling/rescaling method used to generate and sustain turbulence worked as intended. Note that the experimental incoming boundary layer station as defined in Ref. [16] and used here is downstream of the experimental incoming boundary layer station used in the NASA TMR work in Ref. [10].

Figure 4 shows the VULCAN-CFD RANS solution for Mach number. The black dashed line represents a streamwise slice of the ILES computational domain. The left side of the dashed ILES domain, $x/D = 0$, as well as the bottom of the ILES domain from $x/D = 0$ to $x/D = 1.94$ were extracted from the RANS solution to be used as boundary conditions for the ILES. The inflow boundary condition of the ILES used the mean flow properties from the RANS solution in conjunction with a recycling/rescaling method. The RANS solution was interpolated into a 3D boundary condition file which resulted from the 2D axisymmetric RANS solution being rotated about the tunnel axis and point matched on the ILES grid boundaries. The red line shown in Fig. 4 shows the downstream extent of the recycling region for the recycling/rescaling method used to generate turbulent structures in the ILES simulation, $x/D = 1.176$. The blue line shown in Fig. 4 indicates the streamwise station for the experimental incoming boundary layer, $x/D = 1.288$. The shock generator tip is located at $x/D = 0.84$ on the centerline, $r/D = 0$.

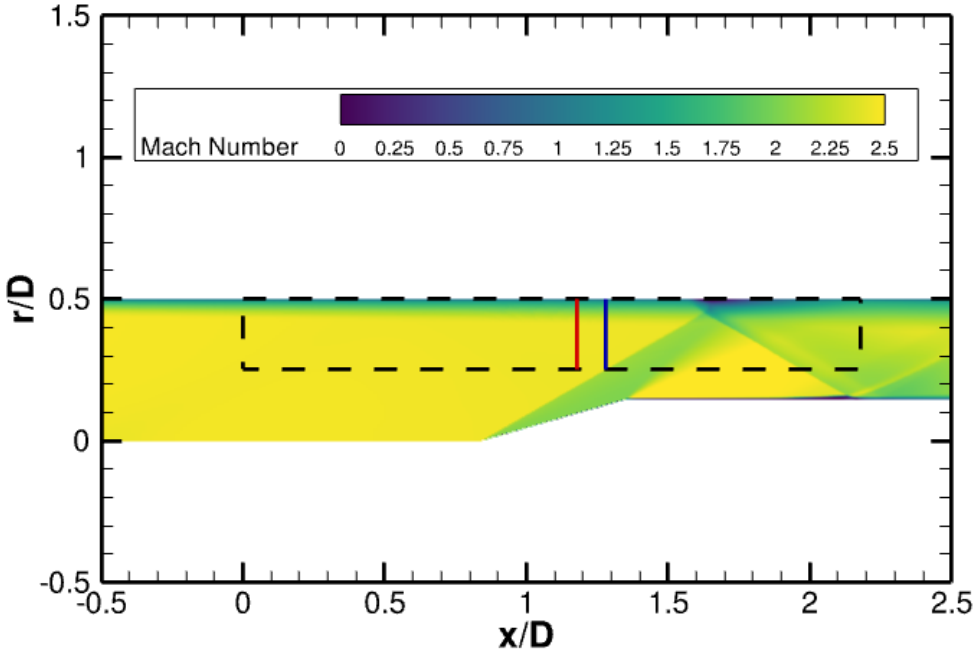

Fig. 4 VULCAN-CFD axisymmetric RANS Mach number solution with the ILES domain shown in dashed black line. Recycling plane is shown in red, and the experimental incoming station shown in blue.

Table 2 Experimental incoming boundary layer comparison, $x/D = 1.288$ [16].

Parameter	Exp (NASA TMR)	Exp	RANS	|RANS Error %|	ILES	|ILES Error %|
Re_D	4.014×10^6	1.007×10^6	9.996×10^5	0.73	1.0003×10^6	0.07
$\delta_{99.5}$ [mm]	11.4	13.7	14.10	2.92	14.30	4.37
δ^* [mm]	2.94	3.90	3.782	3.03	3.662	6.10
θ [mm]	0.79	1.01	0.935	7.42	0.934	7.52

C. ILES Computational Mesh and Boundary Conditions

The structured grid was created by rotating a 2D grid around the axis of the tunnel centerline in Pointwise. The streamwise extent of the domain is 0.37 m, from $x/D = 0$ to $x/D = 2.1765$. The wall normal physical length is 25 percent of the test section diameter, D. The wall-normal and streamwise extent of the ILES domain can be seen in Fig. 4. The reason for not including the shock-generator in the computational domain was computational cost. The domain was selected to be a 25-deg section of the axisymmetric wind tunnel. The azimuthal direction, θ, is defined as in the experimental data with $\theta = 0$ at 12 o'clock and clockwise positive looking in the upstream direction [16]. Poggie et al. [24] found that for compressible, turbulent boundary layer simulations, at least 2 boundary layer thicknesses are needed in the spanwise direction to capture turbulence statistics independent of the domain width. At the wall, there are 2.67 boundary layer thicknesses in the spanwise direction. Computational costs severely constrain the physical size of the computational domain. The grid contains approximately two billion cells. The grid parameters are listed in Table 3. The nondimensionalized grid spacings, compared to those recommended by Georgiadis et al. in Ref. [25], lay in the DNS grid resolution range. The streamwise direction had a constant spacing through the entire domain equivalent to $\Delta x^+ = 8.2$. Of the 1134 points in the wall-normal direction, 621 points are within the incoming boundary layer. Hyperbolic tangent grid clustering was defined from the boundary layer edge to the wall. Above the boundary layer edge, the wall-normal grid spacing is constant at $\Delta y^+ = 3.5$. The first point off the wall was $\Delta y_w = 3.84 \times 10^{-6}$ m. The spanwise spacing varied from $\Delta z^+ = 1.7$ nearest the tunnel centerline and maximum of $\Delta z^+ = 3.5$ at the tunnel wall. At every radius, the spanwise spacing is constant in the azimuthal direction.

Figure 5 shows the boundary conditions of the computational domain highlighted with different colors. The inflow boundary condition consists of prescribed RANS values, and is shown in gray. The mean values are perturbed using the recycling/rescaling method available in VULCAN-CFD. Further details about the recycling/rescaling method can be found in Section II.D. The side boundary conditions are periodic, allowed by the circular test section and axisymmetric positioning of the cone-cylinder shock generator on the wind tunnel centerline. In Fig. 5, the side boundaries are hidden. The downstream boundary is set to extrapolate, and it is shown in red in Fig. 5. The wall of the tunnel is modeled as an adiabatic, no-slip wall and is in green. The adiabatic wall matches the precursor RANS and experimental condition. While the ILES grid does not include the shock-generator, the RANS precursor simulation did, and the effect of the shock and expansion fan are imposed as a farfield boundary condition shown in blue in Fig. 5. The imposed boundary condition stops before the reflected shock leaves the computational domain, allowing that shock to move freely. The yellow portion of Fig. 5 is set to extrapolate to allow the reflected shock to exit the computational domain at a location dictated by the instantaneous flow solution. Vyas [5] used a similar method of imposing a shock as a farfield condition via precursor RANS for the purposes of high-fidelity SWBLI LES calculations.

Time history subdomains were created to collect data at every iteration in the region near the SWBLI. Figure 6 shows the computational subdomains. The subdomains consisted of the tunnel wall and the mid-plane between the periodic boundary conditions. Both regions began at $x/D = 1.44$ and ended at $x/D = 1.99$. The wall domain covered the azimuthal span of the computational domain. The mid-plane domain extended from the wall, $r/D = 0.5$, to $r/D = 0.26$. The insert in Fig. 6 shows an instantaneous density field from the ILES. Iso-surfaces of q-criterion are shown in Fig. 7 to represent some scale of the turbulent structures captured. The view is rotated about the streamwise axis such that the instantaneous separation is visible across the span of the computational domain. The iso-surfaces are colored by streamwise velocity. A transparent instantaneous density field sits in the foreground to show the incident and reflecting shocks' relative positions in the view. Qualitatively the number and spatial density of the turbulent structures increases dramatically downstream of the interaction. The bubble of low-momentum flow at the wall between the shocks is also visible.

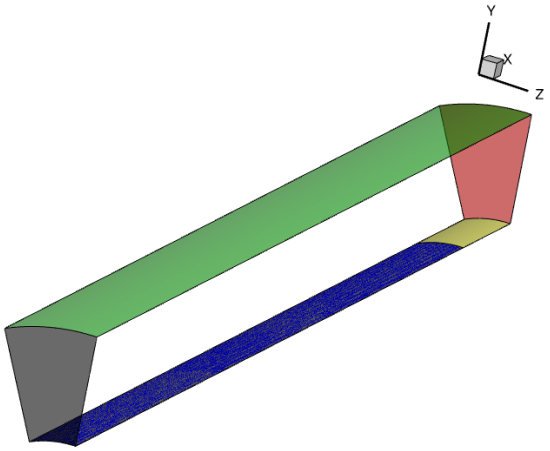

Fig. 5 Computational boundary conditions.

Table 3 ILES grid parameters.

N_x	2781	Δx^+	8.2	$L_x/\delta_{99.5,1}$	26.61
N_y	1134	Δy^+	3.5	$L_y/\delta_{99.5,1}$	3.05
N_z	646	Δy^+_w	0.23	$L_{span,max}/\delta_{99.5,1}$	2.67
N_{tot}	2.037×10^9	Δz^+_{max}	3.5	$L_{span,min}/\delta_{99.5,1}$	1.33

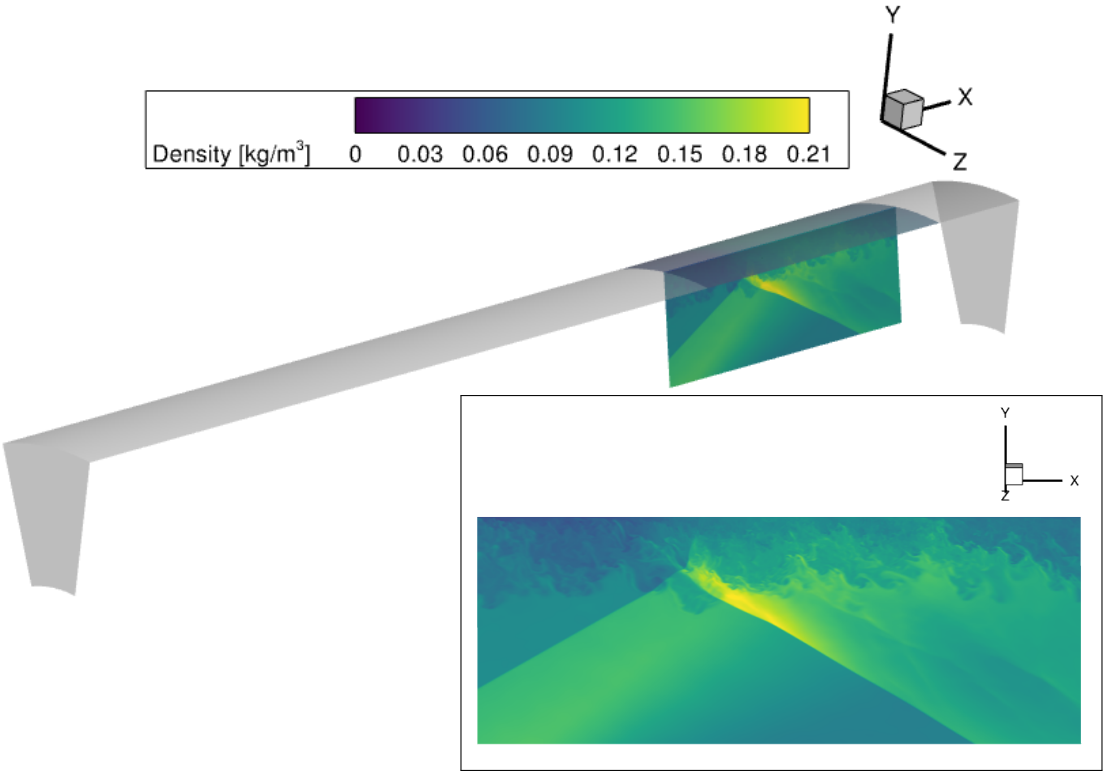

Fig. 6 Instantaneous data collection regions with the computational inflow, outflow and wall for reference. Insert of mid-plane time history subdomain with example instantaneous density contour.

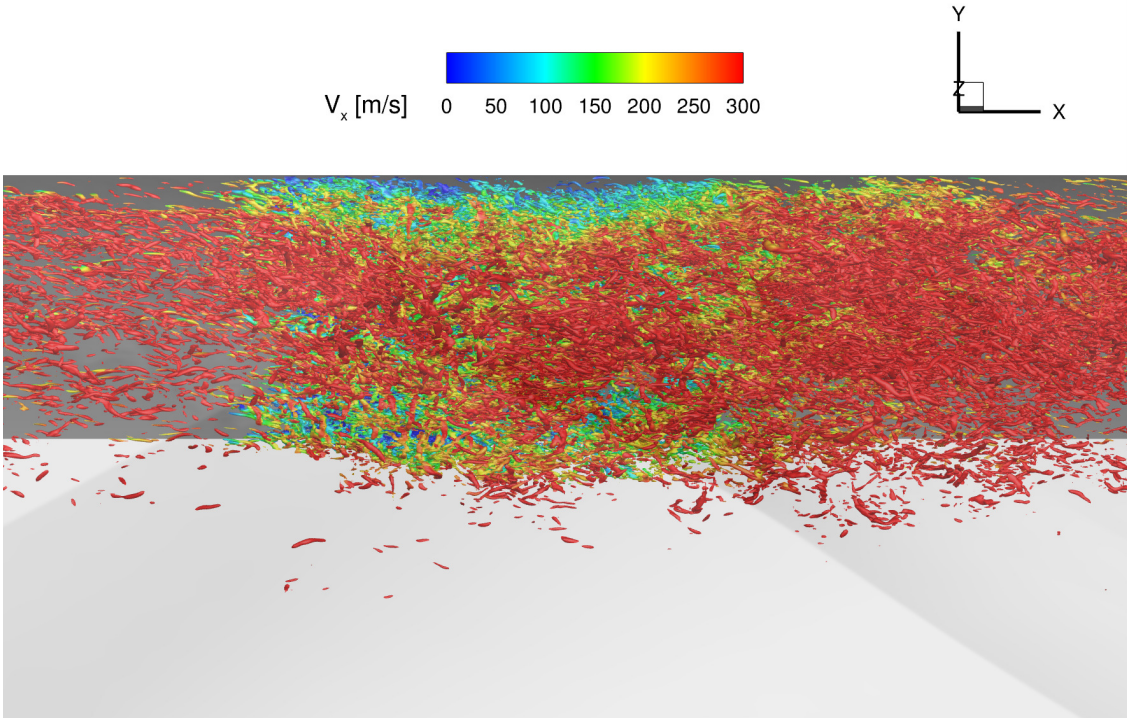

Fig. 7 Iso-surfaces of q-criterion colored by streamwise velocity.

D. VULCAN-CFD ILES Settings

VULCAN-CFD has hybrid RANS/LES and implicit LES options. The present work exclusively uses implicit LES; no subgrid-scale modeling is used. VULCAN-CFD has low-dissipation methods, which it refers to as the hybrid advection schemes, implemented to enable resolution of turbulent content in a scale-resolving simulation. Full details on the low-dissipation schemes implemented in VULCAN-CFD can be found in Ref. [26] with examples of the scheme usage in Refs. [27, 28]. The low-dissipation scheme calculates inviscid fluxes by blending, using a modified form of the Larsson sensor described in Ref. [27], a non-dissipative, symmetric reconstruction with a more dissipative, upwind variable reconstruction when encountering shocks. A fourth-order symmetric reconstruction was paired with a third-order upwind-biased MUSCL scheme using the UNO limiter [29] in this simulation. The viscous fluxes are second-order accurate. The low-dissipation method combined with the recycling/rescaling method described below allow VULCAN-CFD to capture resolved turbulent structures in the boundary layer. White et al. [26] found during the implementation and testing of the hybrid advection methods in VULCAN-CFD that they produced similar solutions to traditional high-order finite-difference codes.

The ILES simulation used a second-order backward-difference scheme with Incomplete LU(0) method with subiterations [30]. The number of subiterations was set to a maximum of 7 to allow flexibility during initialization. After the transients left the domain, the subiterations were ended when the subiteration relative residual error L2-norm was reduced by two orders of magnitude. During the statistically steady state portion of the simulation, the residual error was typically met in 5 subiterations. The physical time step used was $\Delta t = 1 \times 10^{-7}$ s. At the experimental incoming boundary layer station upstream of the interaction, the nondimensionalized time step is $\Delta t^+ = u_\tau^2 \Delta t / \nu_w = 0.17$. On-the-fly ensemble averaging is collected every 5 computational time steps after start-up transients were allowed to exit the domain. The time history subdomains were output every iteration, $f_s = 10$ MHz, once the time history data collection began. Capturing the SWBLI at every iteration in two data planes is a storage intensive operation, but allows for data to be probed spatially and temporally after completing the computational run.

The method of recycling/rescaling is used to generate turbulent content in the simulation. A detailed outline of the recycling/rescaling procedure can be found in Ref. [31]. The essence of the method extracts the fluctuating component of velocity, density and temperature from a chosen recycling location, rescales the values using boundary layer scaling laws, then adds the scaled fluctuations to the prescribed mean flow condition at the inflow location. There are functions implemented in this process which add a random spanwise shift to prevent the creation of large streamwise structures. Additionally an intermittency function is used to not corrupt the freestream. VULCAN-CFD was recently updated to allow recycling/rescaling in pipe flow type configurations as opposed to flat-wall boundary layers. This update allowed VULCAN-CFD to be used for this work. As an initialization condition, the RANS mean values are perturbed once by 20% during the first iteration to initiate scale-resolved turbulent structures faster. The recycling/rescaling region is 0.2 m in streamwise length, from $x/D = 0$ to $x/D = 1.176$, which corresponds to roughly 15 inflow boundary layer thicknesses. The VULCAN-CFD User Manual [20] suggests using at least 8 to 10 boundary layer thicknesses between the inflow and recycling planes. To maintain stability of the simulation, the flow was initialized without the shock imposed. A turbulent boundary layer was allowed to develop via the recycling/rescaling method for 5 domain flow through times, as defined by domain streamwise length divided by the freestream streamwise velocity. The shock was then imposed at the boundary condition and the flow was allowed to adjust for an additional 3 domain flow through times. The total number of iterations for the first 8 flow through times was roughly 48,000. Figure 8 shows the integrated surface friction force in the streamwise direction for the entire simulation. The vertical black line at 48,000 indicates the location which the time averaging process was started. The time history data collection began at 86,000 iterations. The transients due to the starting of the recycling/rescaling method as well as the introduction of the shock boundary condition are seen prior to the initiation of the time averaging and time history data collection. In order to study the low-frequency content common to SWBLI, the simulation was run, with the time history collection on, for approximately 102 cycles of the lowest dominant frequency found in the separation shock foot location. Details are discussed in Section III. The total time history dataset equates to roughly 65 flow through times.

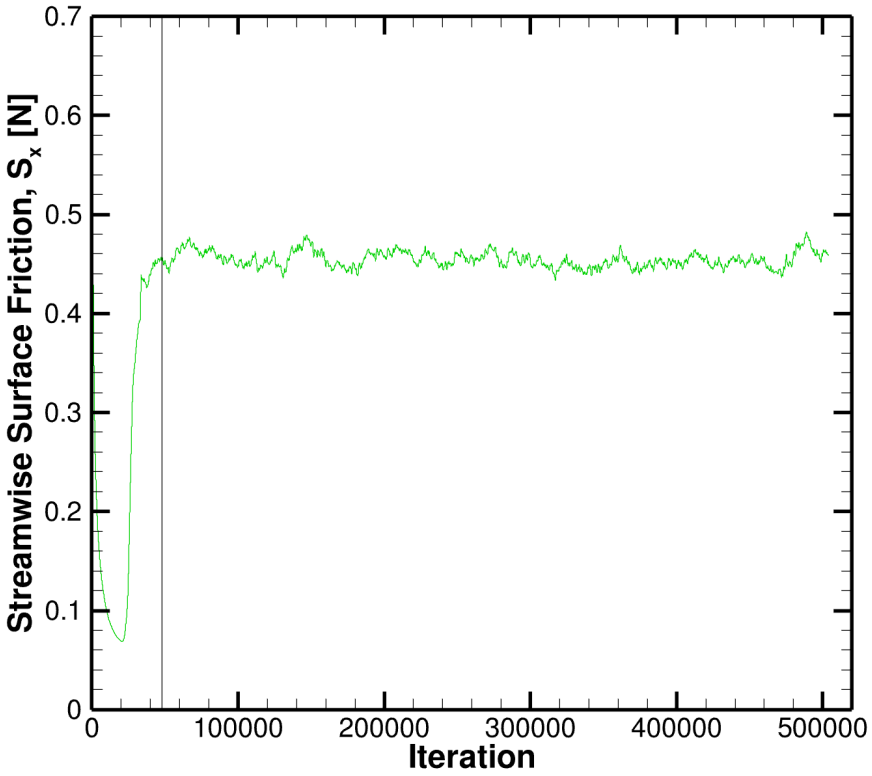

Fig. 8 ILES streamwise friction force time history.

III. ILES Results

A general overview of the flow is presented. Analysis of Reynolds stresses, comparison to experimental data, and PSD analysis follow. A primary focus of the results is comparison with the available experimental data. As previously mentioned, direct comparison to PIV is available, but probe data are at Reynolds number of $\mathrm{Re}_D = 4E6$, four times the ILES Reynolds number. Future works are in progress to attempt matching a higher Reynolds number case in which all measurement types are available.

A. Flowfield Overview

On-the-fly averaging was used to create the time averaged results. The ILES was run for 456,000 time steps, or 0.0456 seconds after time averaging was initiated at iteration 48,000. The volume was then averaged in the spanwise direction due to the axisymmetric nature of the geometry. The volume was sampled in 27 azimuthal planes and averaged, approximately 1 plane per azimuthal degree. The final result, a two-dimensional plane of data, is used throughout the results section unless specified otherwise. Two-dimensional instantaneous figures were taken from the time history subdomain. The averaged data field can be seen in Fig. 9a. The averaging process was allowed to continue running during the collection of the time history subdomains due to the ensemble averaging adding negligible computational expense. During the final 25,000 iterations, the largest percent change in density between solutions in the averaged plane of data was less than 0.1%. The maximum value occurred near the reflected shock foot which is to be expected as that location is prone to low-frequency motion in SWBLI. The maximum error in the average was one to two orders of magnitude lower away from the peak at the reflected shock foot. Power spectral density (PSD) of several locations in the flow, including the reflected shock foot location are discussed below. As a part of the spatially averaging process, the Reynolds stress tensor was transformed from the cartesian coordinates, in which it is solved, to cylindrical coordinates such that the azimuthal average was calculated correctly.

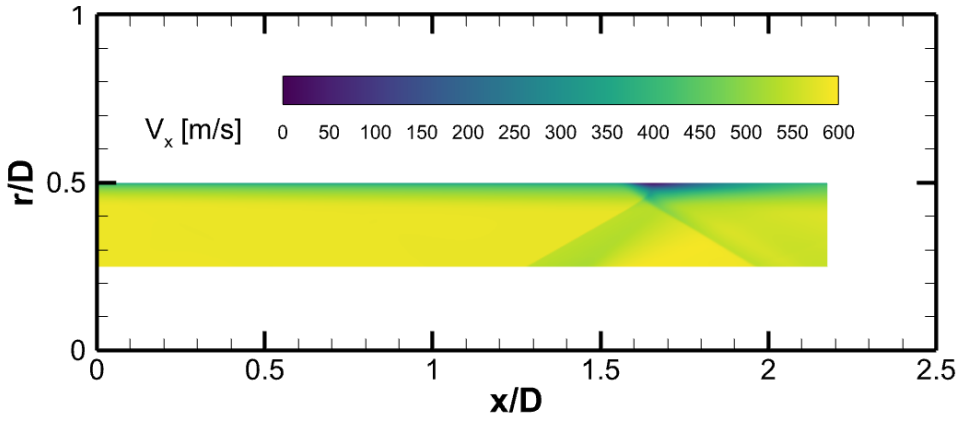

(a)

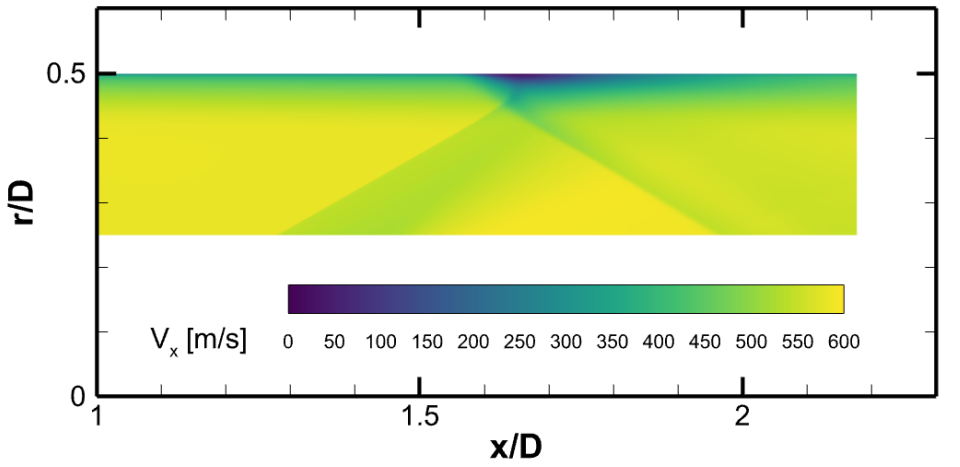

(b)

Fig. 9 (a) Streamwise velocity, spatially and time averaged ILES, full domain, (b) Streamwise velocity, spatially and time averaged ILES, SWBLI view.

As an assessment of the turbulent boundary layer upstream of the SBWLI, Fig. 10 shows the van Driest transformed velocity plotted in wall units. The velocity profile was extracted from the experimental incoming station, $x/D = 1.288$. The coefficients used for the theoretical log law are $\kappa = 0.41$ and $B = 5.1$. The low-dissipation method and the method of recycling/rescaling for sustaining turbulent structures produces a mean velocity profile which lies slightly below the theory in the log law region, but with a similar slope. The viscous sublayer for the ILES agrees with the theory.

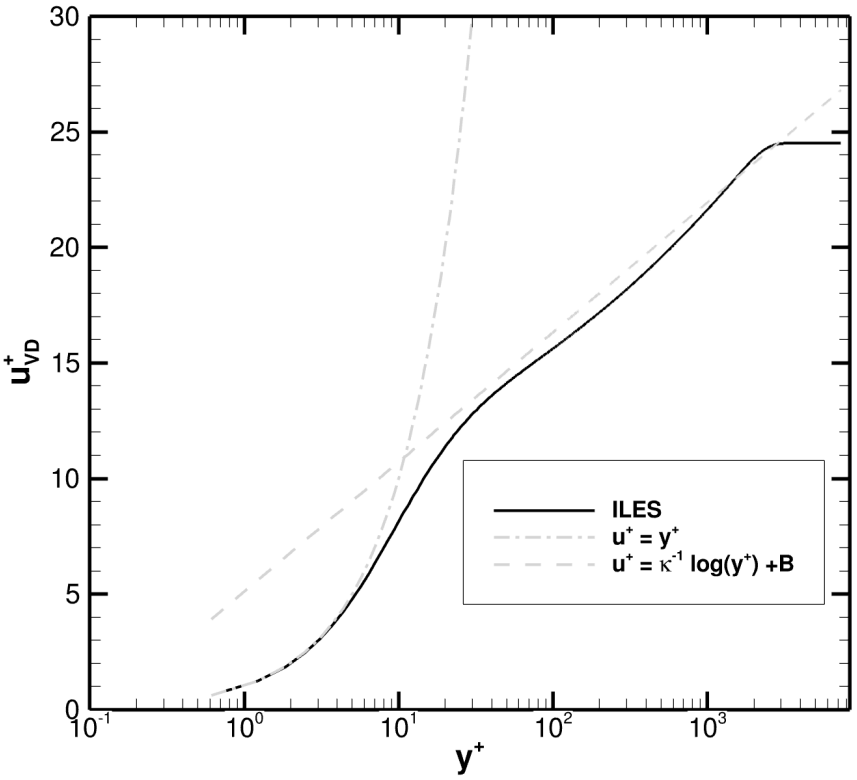

Fig. 10 ILES van Driest transformed velocity profile compared to theory at $x/D = 1.288$.

Figure 11 shows an instantaneous density gradient magnitude of a streamwise slice of the ILES domain. Density gradient magnitude contours are similar to schlieren imaging. The incident and separation shocks are clearly visible. The turbulent boundary layer upstream of the interaction is present. The effect of the expansion fan being imposed at the boundary condition can also be seen. Additionally, weak waves are seen emanating from the boundary layer before the interaction and more strongly after the interaction. The strongest density gradients occur at the incident and separation shocks as well as in the boundary layer directly downstream of the interaction. A weak wave originating from the interaction of the extrapolation boundary condition and the reflected shock is seen. The presence is an effect of the ILES computational domain geometry choice, and a more complex domain shape could be designed to mitigate the effect. Due to the weakness of the wave, its location relative to the SWBLI of interest, and the supersonic nature of the flow, this non-physical flow feature is deemed unimportant.

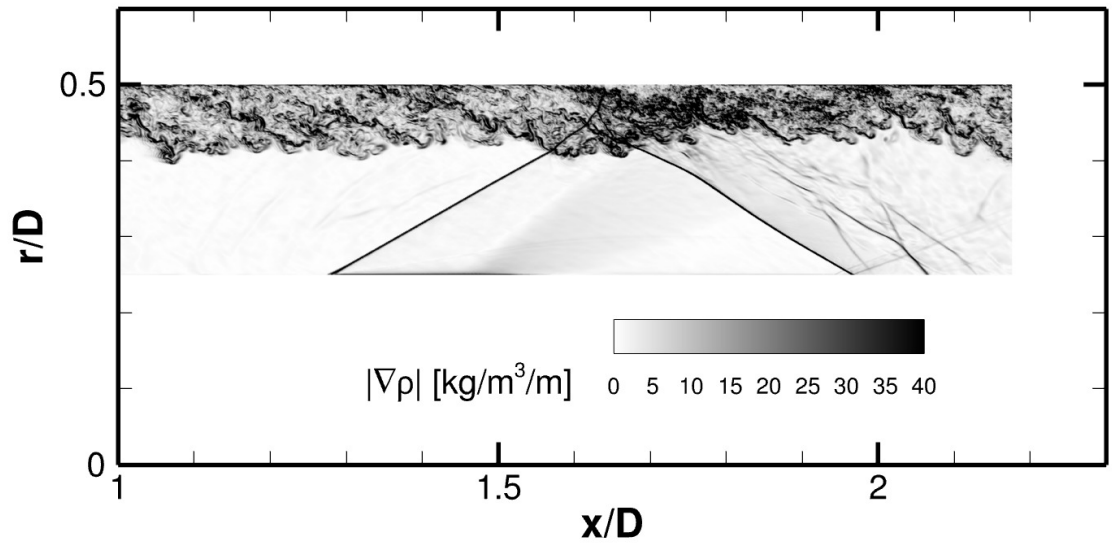

Fig. 11 Instantaneous density gradient magnitude.

The pressure rise through the SWBLI interaction is shown in Fig. 12a. The wall static pressure is normalized by the static pressure at the wall at the incoming station, $P_{w,1}$. For reference, the ILES wall static pressure is $P_{w,1} = 4135$ Pa. The streamwise coordinate is shifted by the inviscid shock impingement location, x_i. The experimental data are normalized by the experimental $P_{w,1}$ and x_i, and the ILES is normalized by ILES values at the equivalent incoming station. In the LES grid units, the inviscid shock impingement is $x_i = 291.2$ mm downstream from the inflow, or $x/D = 1.71$. Additionally the mean reflected shock foot location is roughly $x = 269$ mm downstream from the inflow, or $x/D = 1.58$. The pressure rise begins upstream of the inviscid shock impingement near the location of the reflected shock foot. The ILES performs well compared to the experimental data, with the deviations being a slightly delayed pressure rise and a slightly over predicted peak pressure, either of which could be partially due to uncertainties in the parameters used for nondimensionalization. Fig. 12b shows the RMS of the wall pressure fluctuations, $\sqrt{\overline{p'^2}}$ divided by the wall static pressure at the experimental incoming station. Double peaks are seen at roughly $x - x_i = -20$ mm and $x - x_i = -11$ mm. Additionally, the return to the upstream value is not reached in the time history subdomain. Downstream of the interaction shows a similar trend to the averaged static pressure profile which takes nearly 100 mm from the inviscid shock impingement to recover. A similar double peaked RMS pressure plot is seen in the computational work by Bernardini et al. [32] and associated experimental work by Dupont et al. [33] at Mach number 2.3. That work shares the characteristic with the present work of two separated regions based on spatially and temporally averaged streamwise skin friction coefficient, which will be discussed next.

The streamwise skin friction coefficient, C_{fx}, is shown in Fig. 13 to help understand the separation behavior of the SBWLI. The plot is again shown shifted by the inviscid shock impingement location. Near $x - x_i = -300$, there is an rapid change before the curve stabilizes near a constant value. This is a nonphysical portion of the solution at the inflow condition as the recycling/rescaling introduces turbulent structures into the inflow. Moving downstream from the inflow by roughly $2.5\delta_1$ the turbulent boundary layer has stabilized to a nearly constant skin friction coefficient which decreases slightly as the boundary layer thickness grows downstream. Then near $x - x_i = -30$ mm or roughly $x/D = 1.53$ the effect of the reflected shock foot can be seen quickly dropping the C_{fx} towards negative values, an indication of separation. Often in SWBLI, the interaction is strong enough such that the flow remains separated in the space between the reflected shock foot and the inviscid shock impingement location. However, the current freestream conditions provide an interesting edge case where mean C_{fx} suggests the flow reattaches between these two separation bubbles but separates again at the inviscid shock impingement location. Using $C_{fx} = 0$ as an indication of flow separation, the flow separates from $x - x_i = -22.6$ mm to $x - x_i = -19.2$ mm and $x - x_i = -11.3$ mm to $x - x_i = -8.5$ mm, or $0.16\delta_1$ and $0.19\delta_1$ respectively. The interaction length scale will be defined as the first $C_{fx} = 0$ location to the inviscid shock impingement. Reevaluating the double peaks in RMS pressure fluctuations in Fig. 12b, it can be inferred that the increased fluctuation intensity is related to the separation bubbles caused at shock impingement locations.

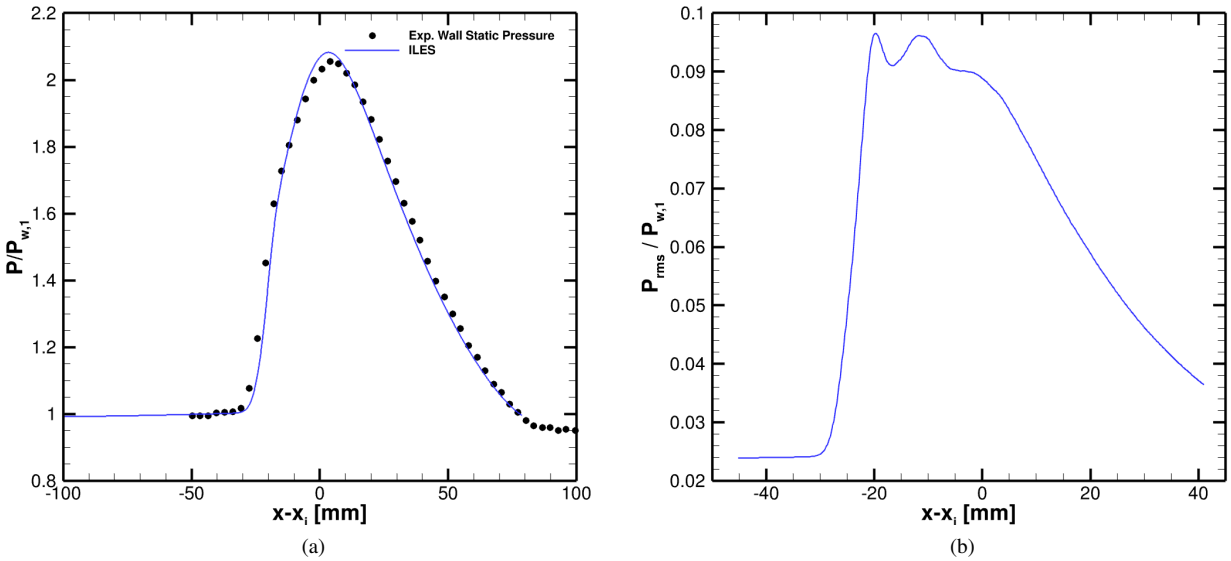

Fig. 12 (a) Wall static pressure profiles, spatial and temporally averaged, (b) RMS pressure fluctuations, spatially and temporally averaged.

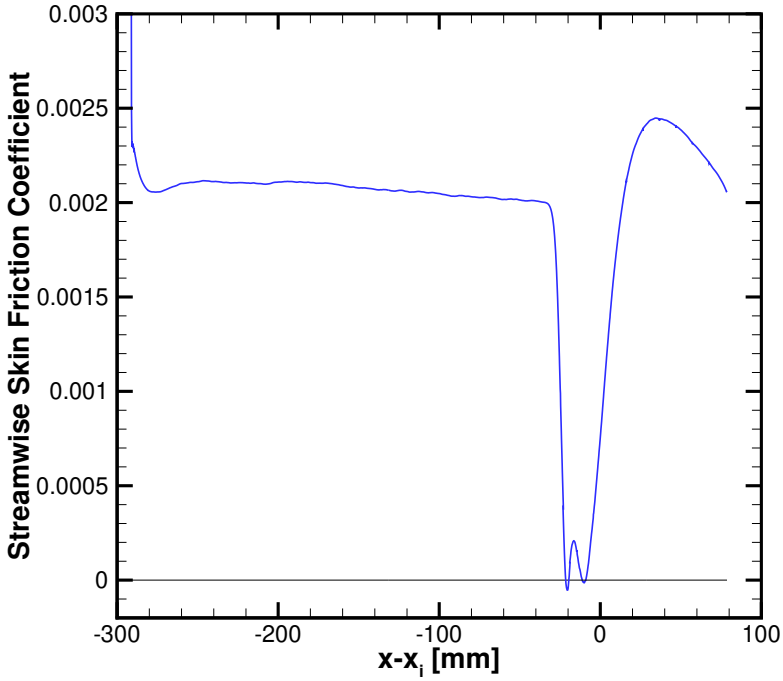

Fig. 13 Streamwise skin friction coefficient, spatial and temporally averaged.

The space-time averaging of the skin friction coefficient does conceal some interesting features of the flow which viewing the entire wall reveals. Figures 14-15 show the instantaneous and time averaged wall from the ILES. The spanwise direction has been unwrapped consistent with the experimental azimuthal convention of 12 o'clock and clockwise positive looking in the upstream direction. The view presented is looking at the unwrapped wall from the perspective on the tunnel centerline. The region in both plots where the streamwise skin friction coefficient is below zero has been outlined in purple. Looking at the instantaneous C_{fx}, a prominent streaky pattern is seen in the turbulent

boundary layer upstream of the interaction. In this instantaneous snapshot, the intermittency of the separation is clear. Within the interaction, the C_{fx} alternates sign multiple times along a spanwise or streamwise line. In comparison, Fig. 15 shows distinct bubbles. There is first a spanwise bubble which is nearly unbroken which represents separation downstream of the reflected shock foot. Downstream there is a variation in the span between regions of positive and negative C_{fx}. The area of research focusing on spanwise variation of large-scale turbulent structures in pipe flows could lead to an explanation, but more analysis is required [34]. Due to the azimuthal variation, in the time average, there are some azimuthal stations which have a connected separation bubble and some stations which there are two distinct separation regions as seen in Fig. 13 which is the azimuthal average of Fig. 15.

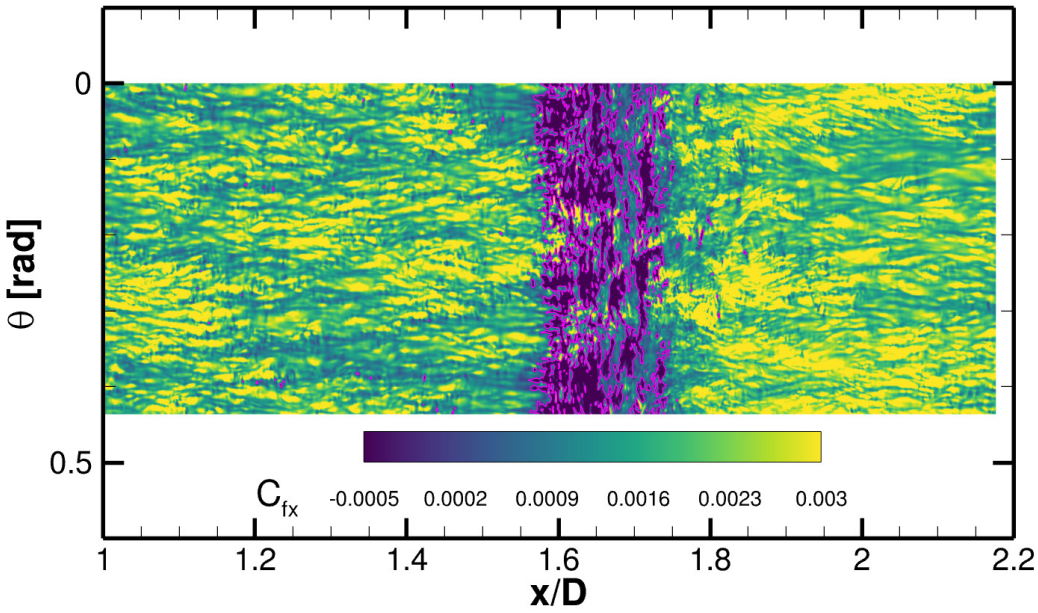

Fig. 14 Instantaneous streamwise skin friction coefficient.

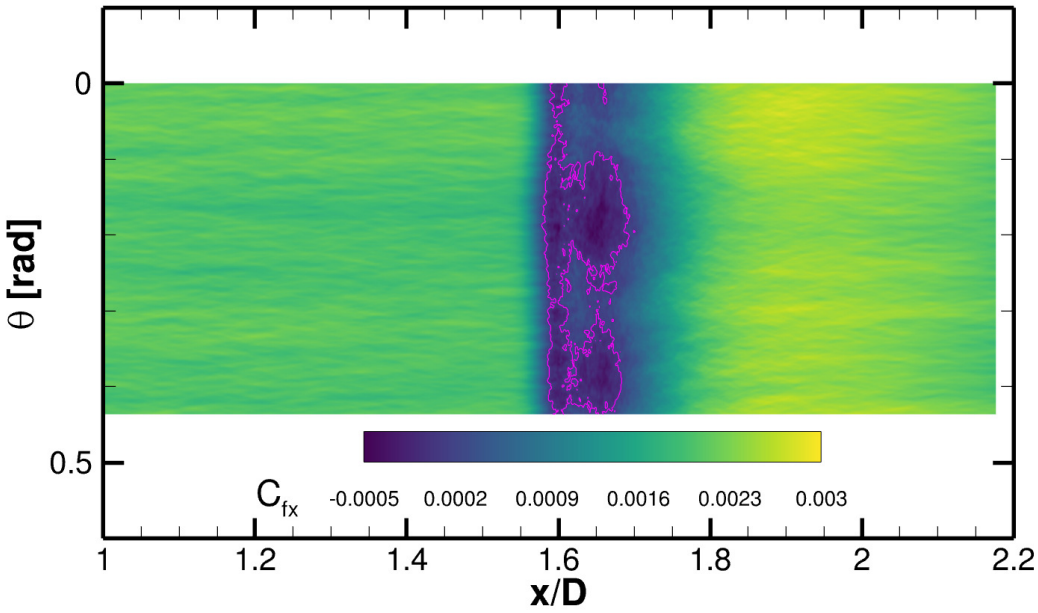

Fig. 15 Streamwise skin friction coefficient, temporally averaged.

The wall normal velocity, Fig. 16 is defined as positive in the wall normal direction, toward the wind tunnel centerline. As a reminder, the tunnel wall is at $r/D = 0.5$. The expected flow turning occurs after each shock. The incident shock turns the flow towards the wall. The wall normal velocity contour also shows the influence of the expansion fan which is imposed via boundary condition which experimentally emanates from the shoulder of the cone-cylinder shock generator turning the flow back towards the axis of the tunnel. At the wall between the shock impingement points, the flow is moving away from the wall. This can be seen qualitatively in Fig. 7. The flow is being forced up away from the wall due to the presence of the low-momentum flow in the interaction region. The reflected shock then also turns the flow back towards the centerline. The pattern of flow turning is the expected result and qualitatively agrees with the NASA TMR case being developed with RANS and associated PIV at a higher Reynolds number, $\mathrm{Re}_D = 4E6$, seen in Figure 37 of Friedlander et al. [10].

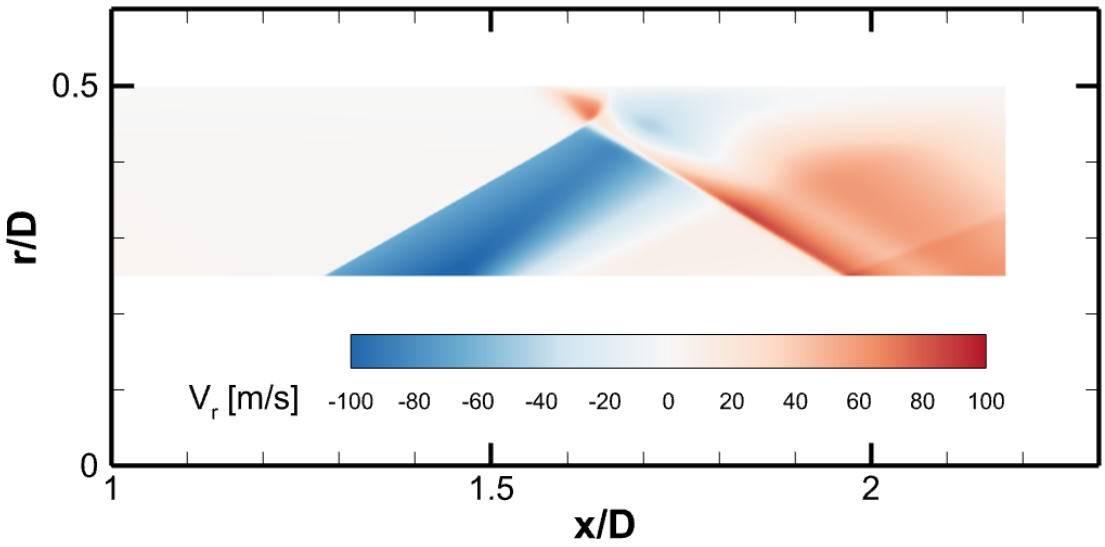

Fig. 16 Wall normal velocity, spatial and temporally averaged.

B. Reynolds Stresses

Figures 17-19 show components of the Reynolds stress tensor normalized by the incoming station freestream streamwise velocity, $< (V_x)_{1,\infty} >$. Figures 17 and 19 have direct equivalents in Figures A8.a and A9.a in Ref. [16]. Figure 19 of Reising and Davis [14] shows plots of all three quantities for a higher Reynolds number of $\mathrm{Re}_D = 2E6$ as opposed to the current work at $\mathrm{Re}_D = 1E6$. The contours agree well with the trends seen in the previously published data. Direct comparison for these quantities will be done using line plot extractions of the experimental and ILES contours, see Figs. 21-26.

Figure 17 shows the normalized variance of the axial velocity. The peak values occur in the region slightly above the two separation bubbles. The $\overline{V_x'V_x'}$ peak moves from closer to the wall near the reflected shock foot location to further from the wall near the inviscid shock impingement location. The line of peak $\overline{V_x'V_x'}$ is at an angle of roughly 13° relative to tunnel axis. For reference, the incident shockwave via the conical shock relations has an angle of roughly 29°, and was verified in the ILES by measuring the mean shock angle in Tecplot. This lifting of the variance of the axial velocity likely follows the shear layer created from the reflected shock foot separation bubble. While the incident shock is only visible in the $\overline{V_x'V_x'}$ field near the boundary layer edge, the reflecting shock is visible out into the freestream. This behavior is similar to the corresponding PIV figures seen in [14, 16]. The reflected shock is less steady due to the unsteadiness inherent in the bubble region at the origin point for the shock, but the incident shock is generated steadily from the shock generator in the experiment and from the boundary condition in the ILES. The incident shock only becomes visible in this time averaged view once near the boundary layer edge which perturbs the shock foot as it approaches the wall. The $\overline{V_x'V_x'}$ peak decays quickly down to a level similar to upstream in $3.6\delta_1$ measured from the $C_{fx} = 0$ reflected shock foot position. Figure 18 shows the variance of the wall normal velocity, and Fig. 19 shows the shear component. Comparing the decay of the variance of the streamwise velocity to the decay of the wall normal, $\overline{V_r'V_r'}$, or shear component, $\overline{V_x'V_r'}$, it is clear the streamwise component relaxes the fastest. This behavior agrees with PIV

results in Ref. [16]. The $\overline{V_r'V_r'}$ and $\overline{V_x'V_r'}$ relax to near upstream levels near the end of the computational domain $6.1\delta_1$ downstream of the $C_{fx} = 0$ reflected shock foot position. Similarly to the $\overline{V_x'V_x'}$ component, the line of peak $\overline{V_r'V_r'}$ has an angle of approximately 13° relative to tunnel axis beginning at the reflected shock foot location. However, once the line of peak $\overline{V_r'V_r'}$ reaches the intersection with the incident shock, the greatest values of $\overline{V_r'V_r'}$ becomes axially aligned with the tunnel again. In the shear stress component, Fig. 19, in addition to seeing shear magnitude increase across the two shocks, this contour shows a weak expansion just downstream of the incident shock. This feature is seen in the PIV contours, Figure A9, of shear stress in Ref. [16]. In the region near the wall in the interaction, the line of peak negative shear was estimated to have an angle relative to axial of roughly 6.5°. This is half the angle seen in the lines of greatest change in the streamwise and axial components. A closer view of the interaction region is shown in Fig. 19b.

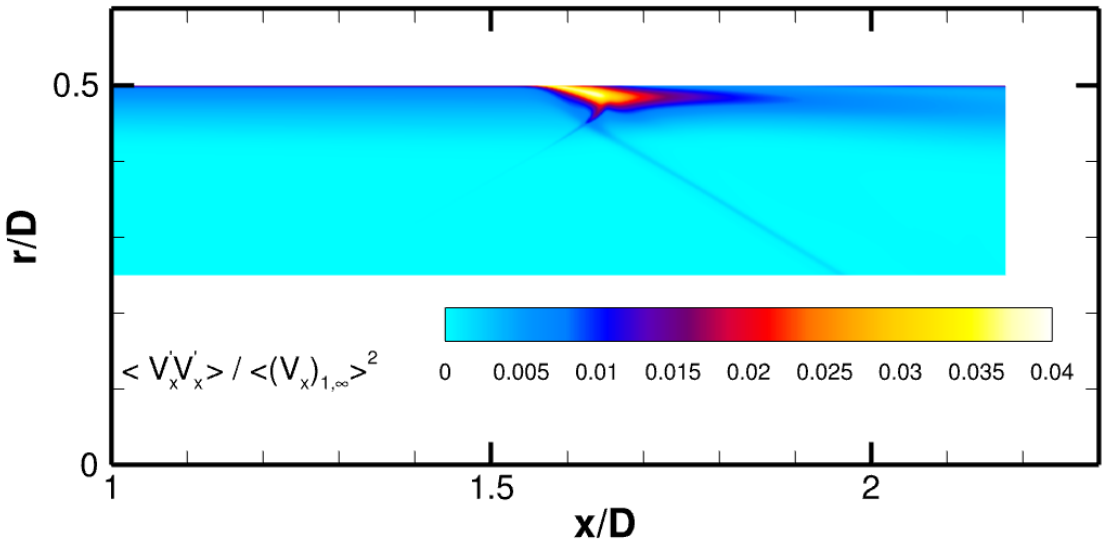

Fig. 17 Variance of streamwise velocity, spatial and temporally averaged.

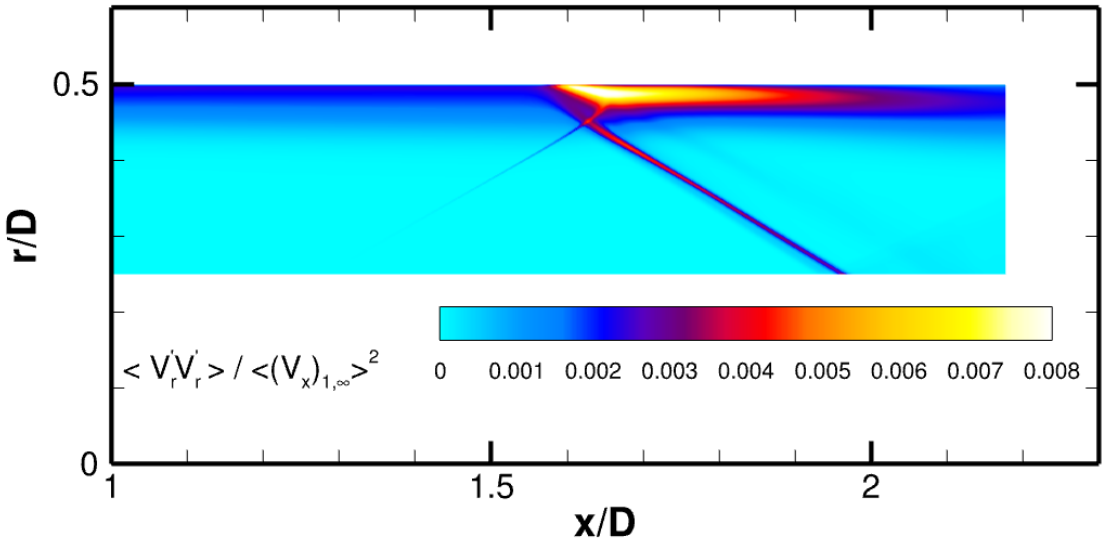

Fig. 18 Variance of wall normal velocity, spatial and temporally averaged.

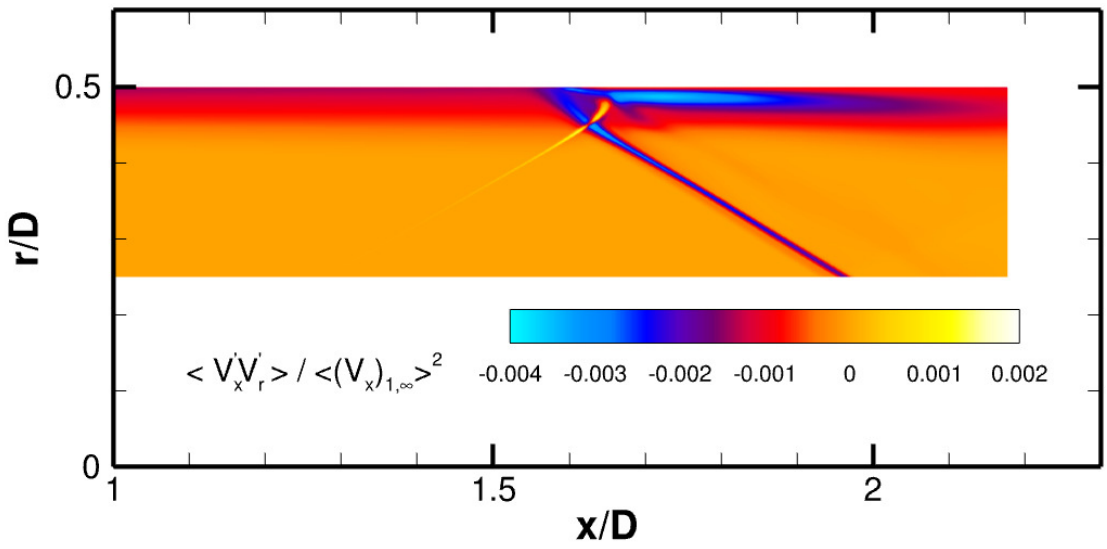

(a)

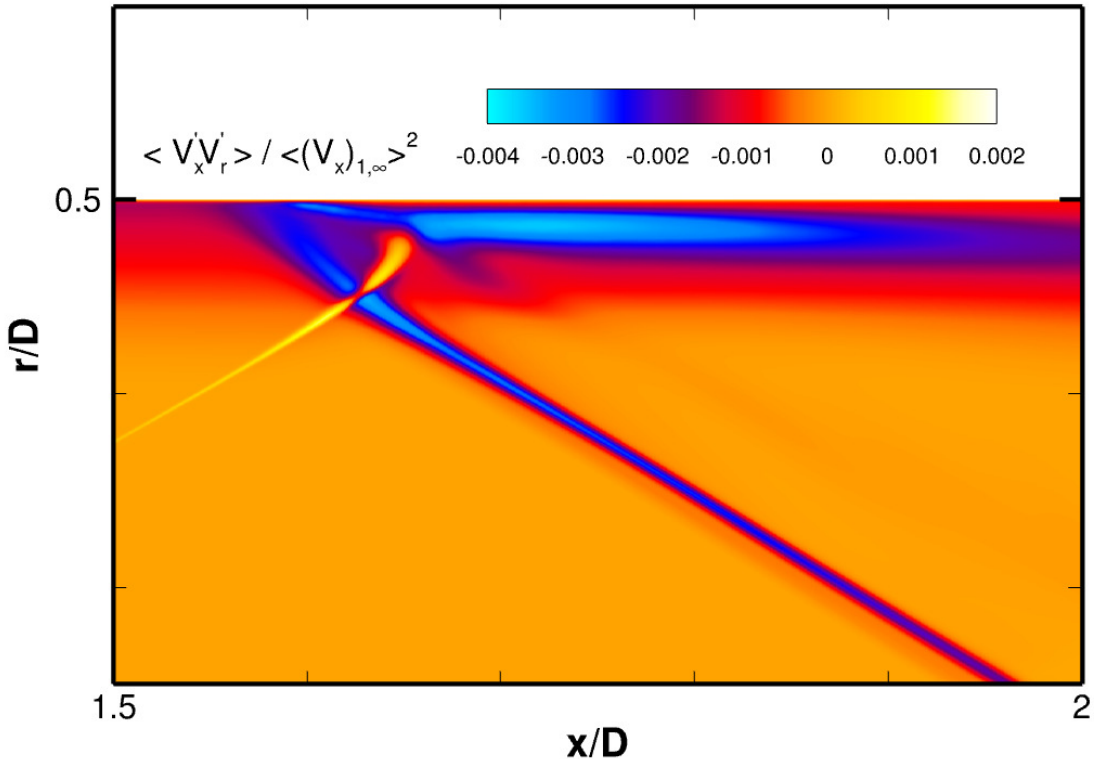

(b)

Fig. 19 (a) Shear stress contour, spatial and temporally averaged, (b) Narrow SWBLI view.

C. Experimental Profile Comparison

Figure 20 and Table 4 provide a reference for the forthcoming line plot comparisons to experimental data and PSD analysis. The locations in Table 4 were determined from the ILES time and spatially averaged data. The reflected shock foot location was probed at several locations, R1-R3. The streamwise extent of the data presented here focuses on the interaction region, but additional PIV stations are publicly available in the data files provided by Reising with Ref.

[16] on the NASA Technical Reports Server. Figures 21-26 are line plot extractions of experimental data compared to the present ILES. Note the data are flipped vertically for clarity with the convention of placing the wall at the bottom of the vertical axis of a line plot. As previously mentioned, only PIV is available at the ILES Reynolds number. Completing ILES cases at additional conditions with probe data is in progress and will be documented in a future work. However, where possible, additional data are presented from other experimental data collected during the TCFDVE test campaign. Higher Mach number simulations with stronger SWBLI are also a target for future work to compare to the HMVE test campaign that followed the TCFDVE. To attempt to collapse data with differing Reynolds number, the wall normal direction is normalized by the displacement thickness at the incoming station. In addition to those displacement thicknesses found in Table 2, the PIV data at $\mathrm{Re}_D = 2E6$ was normalized by $\delta^* = 3.33$ mm from Table 3 of Ref. [16]. For experimental comparisons, the normalizations use freestream values at the incoming station. Experimental data are normalized by the experimental freestream values, and the ILES data are normalized by the ILES freestream values. The data are extracted at the same physical stations for the PIV data and ILES as the Pitot and hot-wire probe rakes. The data are plotted by shifting the streamwise station by a scalar multiplied by the quantity of interest to allow for the details of the curves to be seen. The streamwise station at which the data are taken is listed above each set of curves in mm.

Table 4 Useful streamwise locations in the flow.

Location	Probe Label	$x - x_i$ [mm]	x/D
Incoming Exp. station, x_1	-	-72.1	1.288
Time history upstream probe	U	-45.2	1.44
Reflected shock foot, initial pressure rise	R1	-29.4	1.54
Reflected shock foot, pt. 2	R2	-26.1	1.56
Reflected shock foot, $C_{fx} = 0$	R3	-22.6	1.58
Minimum C_{fx}	Cf	-9.5	1.65
Incident shock inviscid impingement	I	0.0	1.71
Time history downstream probe	D	28.8	1.88

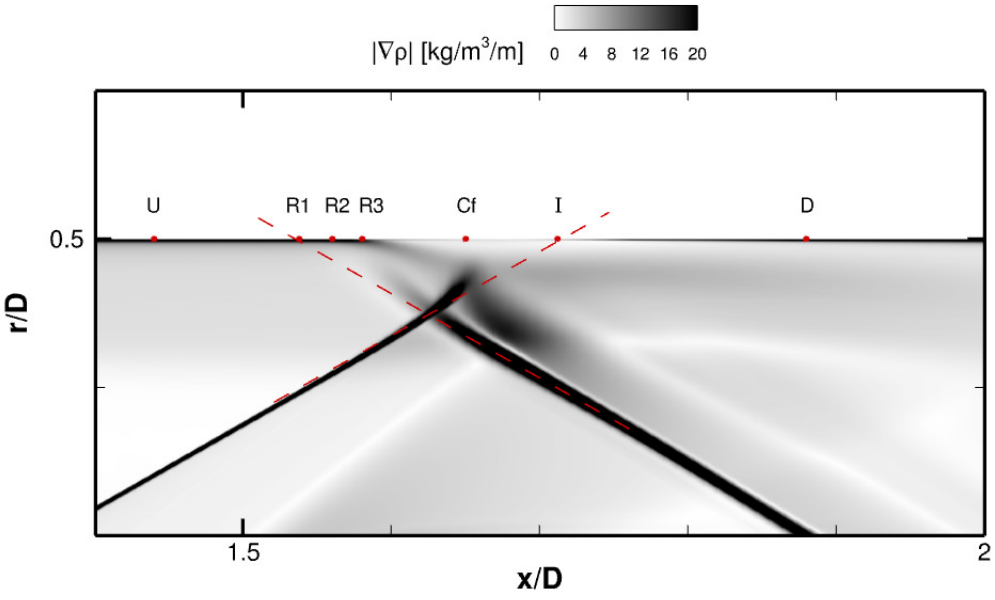

Fig. 20 Time averaged density gradient magnitude with station references for PSD locations.

Reising discusses in Ref. [16] that the spatial scaling by displacement thickness is not completely successful in collapsing PIV data through the interaction. As can be seen throughout Figs. 21-26, the PIV profiles before and after the interaction tend to collapse well. However, the data in the interaction region tends to appear to have a wall normal

shift when comparing between Reynolds numbers. Reising notes that using only an outer scale, boundary layer length scales, will not collapse the data because the ratio of inner and outer scales in the interaction depends on Reynolds number. At lower Reynolds number, Reising found that the shear layer above the separated region lifts further from the wall shifting the profiles away from the wall. Interestingly, at the higher Mach numbers tested experimentally in the HMVE test campaign the influence of the lower Reynolds number decreased and the profiles collapsed better through the interaction; see Ref. [16].

Generally in Figs. 21-24 the ILES matches best with the PIV at the $\mathrm{Re}_D = 4E6$. Additionally, the two lower Reynolds number datasets for the PIV collapse well. This trend holds especially well for Figs. 21-23. The pattern can still be seen in the shear stress in Fig. 24, but the LES and $\mathrm{Re}_D = 4E6$ PIV data have marginally worse agreement. Even the shear component of the Reynolds stress, which shows the most disagreement, begins to collapse again downstream of the inviscid shock impingement location. The desired result would show best agreement between the LES and PIV at the same Reynolds number. The reasoning for this grouping is not clear. Perhaps different scaling options could better collapse some of the data. There could be an experimental unknown at the lower Reynolds number which is not fully understood. Reising does discuss the limitations of the PIV viewing angle given the circular test section, and some PIV seed oil pooling issues near the separation region. Perhaps at the lower tunnel pressures, these issues could be more pronounced. The LES closely matching the PIV at the highest Reynolds number motivates running additional ILES cases to match the available data at the higher Mach number and Reynolds number combinations of the followup experiential campaign. Those cases had better collapse of the PIV profiles, so if the ILES is able to match at those conditions, it might elucidate reasons for the unexpected PIV data collapse groupings seen in this work. As the current case approaches several computational limitations for the authors, computational resolution will need to be traded to achieve higher Reynolds numbers.

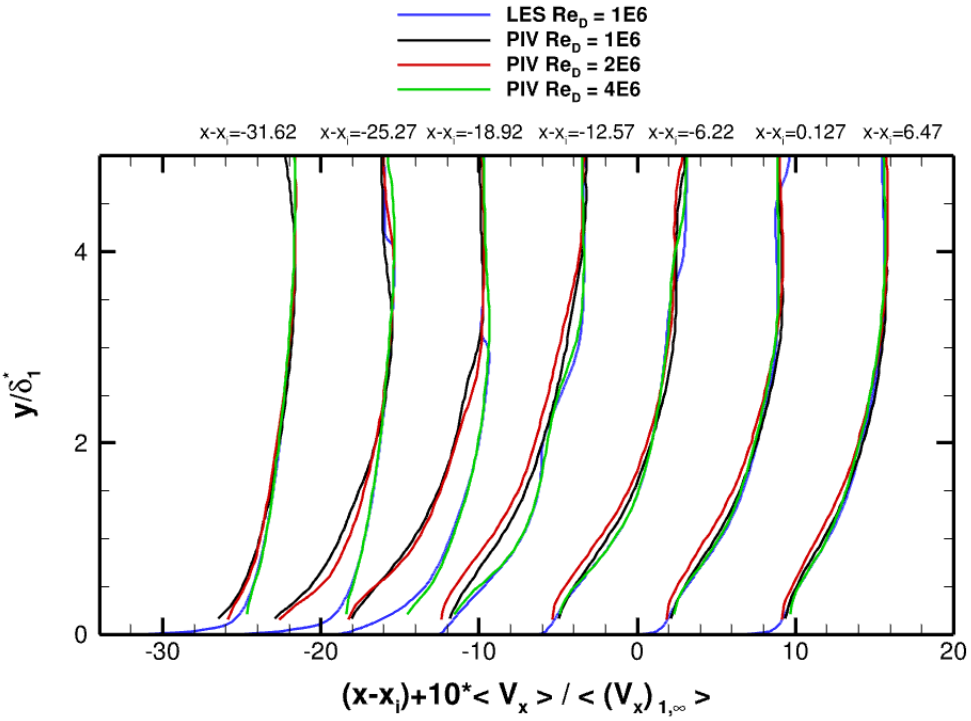

Fig. 21 Streamwise velocity, ILES and PIV at probe stations.

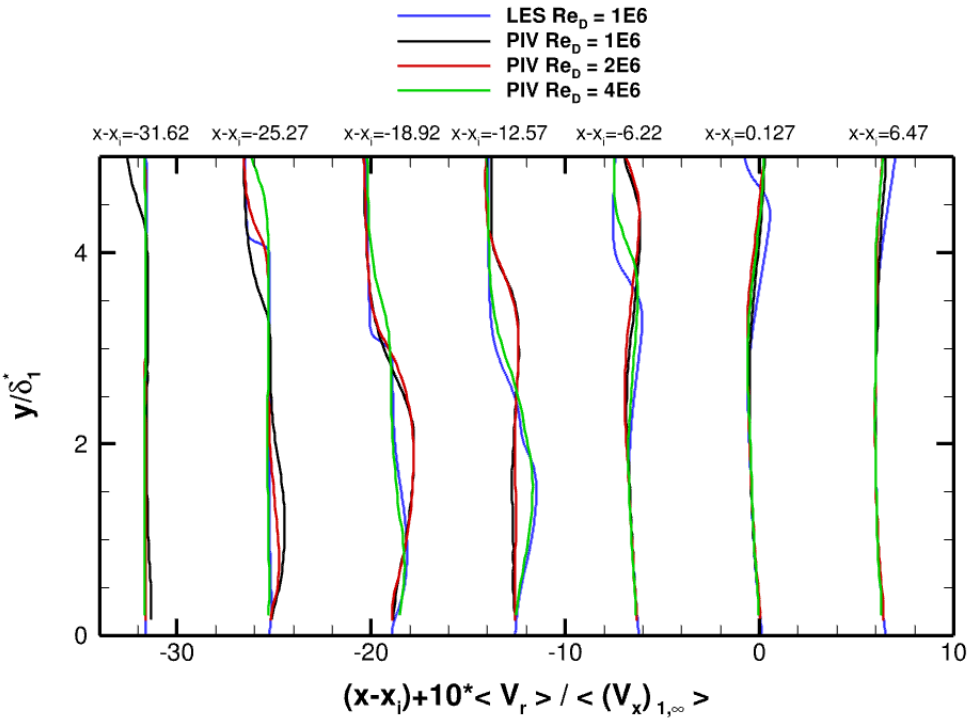

Fig. 22 Wall normal velocity, ILES and PIV at probe stations.

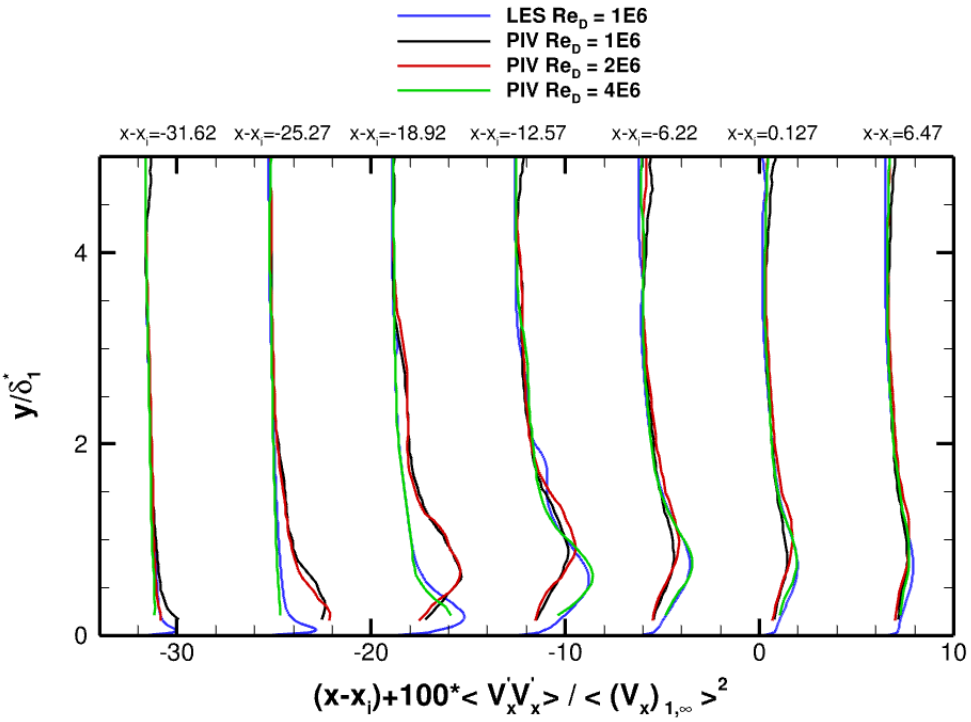

Fig. 23 Variance of streamwise velocity, ILES and PIV at probe stations.

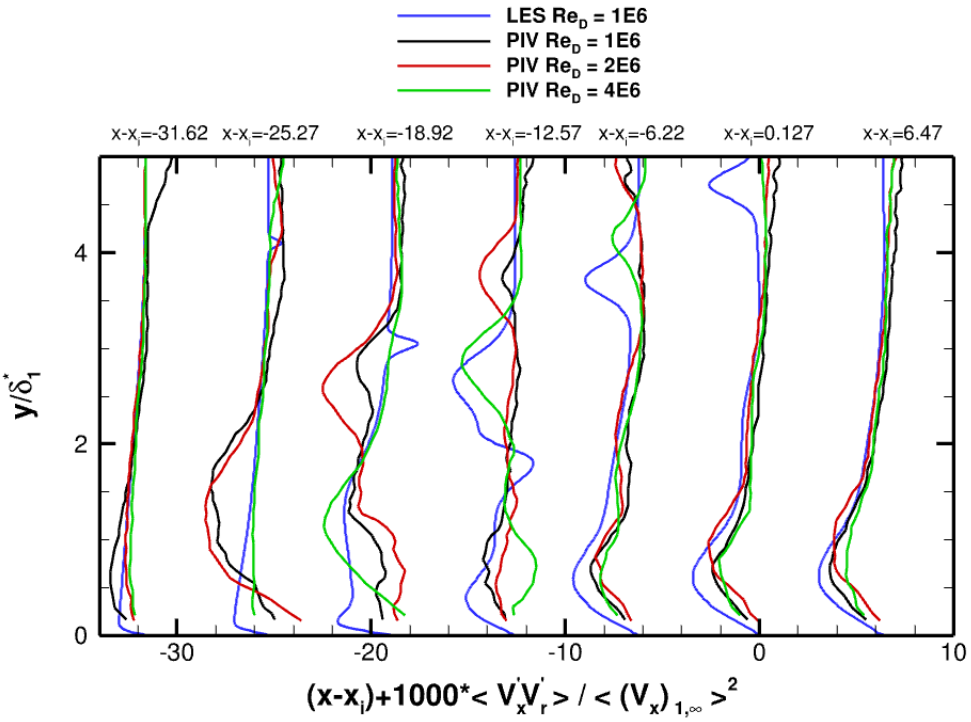

Fig. 24 Reynolds shear stress, ILES and PIV at probe stations.

In addition to matching the PIV well, Figs. 25-27 show good agreement between ILES at $\mathrm{Re}_D = 1E6$ and Pitot and hot-wire data at $\mathrm{Re}_D = 4E6$, Refs.[11–13]. A slight mismatch of the angles of the incident and reflecting shocks likely is affected by the choice of outer scale normalization for the wall normal direction. The outer scale normalization would not be expected to scale the inviscid behavior of the shocks well, given the shock angles in the freestream should be the same for the same freestream Mach number. The profiles of total pressure measured by the Pitot rakes through the interaction approach the wall increasingly vertically, an indication of separated flow. There is a clear concavity sign change near the wall when examining, for example the $x - x_i = -25.27$ and $x - x_i = -6.22$ rakes. The mass flux curves do not agree quite as well with the ILES as the Pitot profiles do. Figure 26 shows the hot-wire measured mass flux as well as the time averaged ILES mass flux. The hot-wire curves below roughly $y/\delta^* = 1.5$ begin to diverge from the LES curves. The furthest upstream curve matches the furthest towards the wall. However, unlike many of the previous figures, downstream of the interaction the hot-wire and ILES do not seem to collapse again. Figure 27 shows the mass flux turbulence intensities at the same stations as the mass flux data. Near the wall and upstream of the interaction the turbulence intensity of the LES is lower than the experimental data. Near the wall through the interaction and downstream of the inviscid shock impingement, the LES and hot-wire data agree more closely. The upstream profiles tend to be more uniform vertically, but throughout the interaction and downstream the profiles have increased turbulent intensity at a wall value of roughly $y/\delta_1^* = 1$ before decreasing approaching the wall.

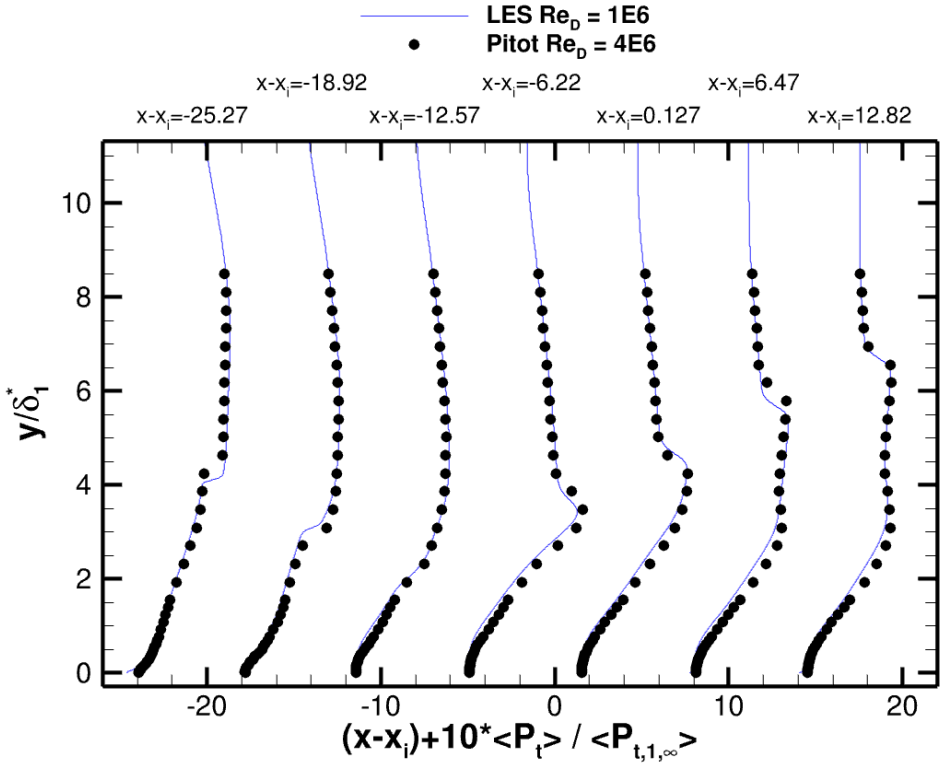

Fig. 25 Total pressure, ILES, and Pitot at probe stations.

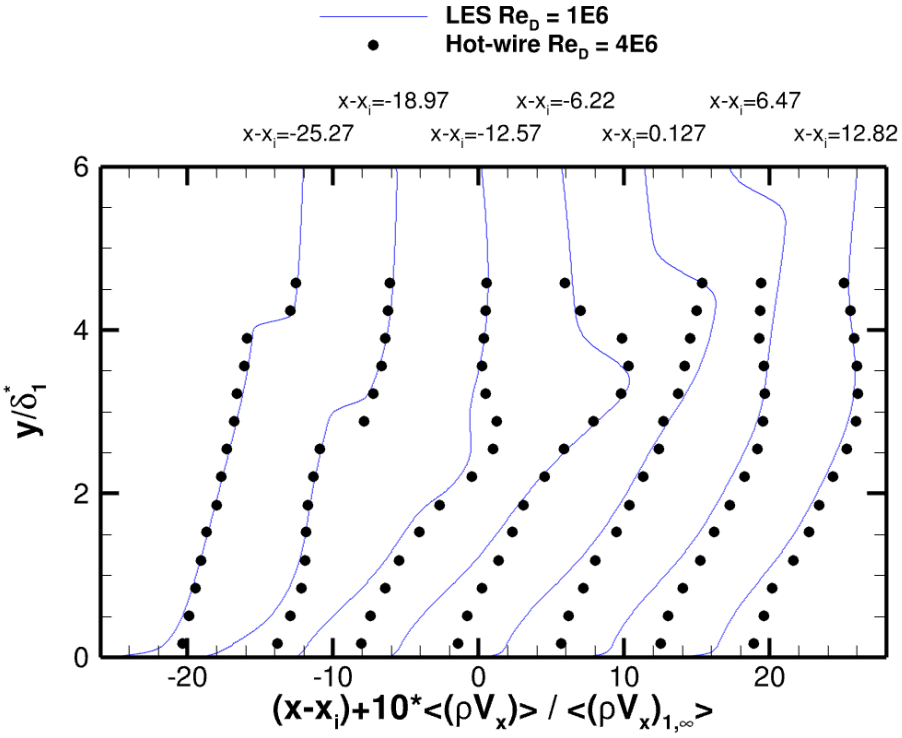

Fig. 26 Mass flux, ρV_x , ILES, and hot-wire at probe stations.

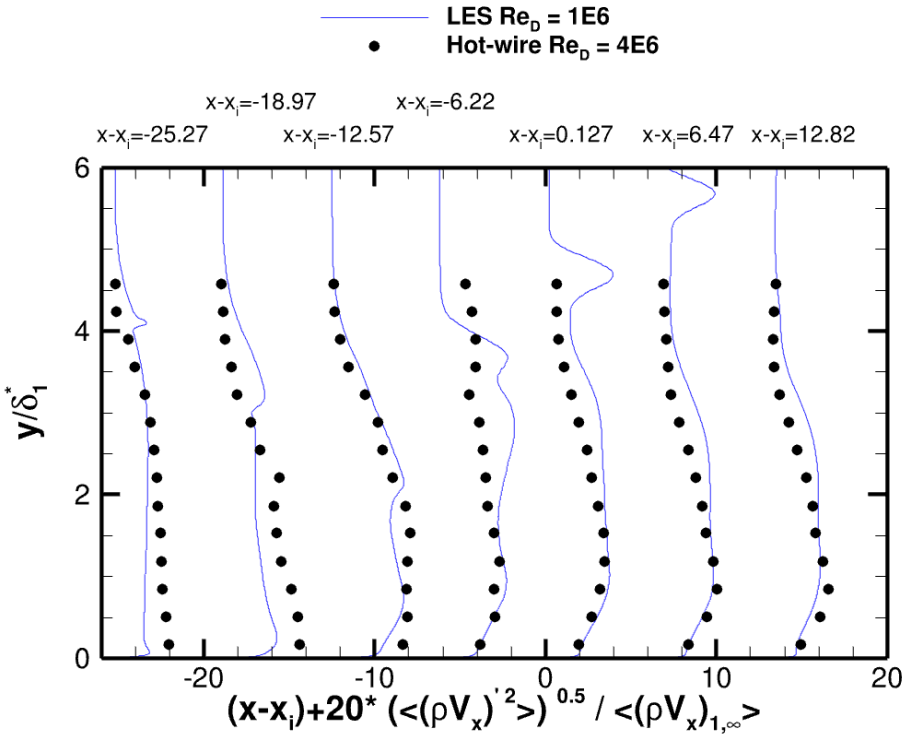

Fig. 27 Mass flux turbulent intensity, $\sqrt{\overline{(\rho V_x)'^2}}$, ILES, and hot-wire at probe stations.

D. Power Spectral Density

Power spectral density plots created using time series data of pressure from the wall subdomain near the SWBLI are shown in Fig. 28-31. The labels in the legends refer to Table 4. The wall subdomain can be seen in Fig. 6. There are several benefits from extracting the time series for the wall subdomain. The first benefit is probe locations can be evaluated after completing the simulation as opposed to making educated guesses for locations of interest prior to running the simulation. The second benefit is that given the axisymmetric nature of the flow, data can be extracted from many points at the same axial station and effectively increase data sample size. For all PSD shown, data were sampled at 65 azimuthal stations. The PSD for each station were created then all were averaged. This process greatly improved the PSD quality, producing smoother data. The PSD was done on the fluctuation pressure data over time. The Matlab function pwelch was used with eight bins with 50% overlap and Hamming windowing. The frequencies have been nondimensionalized to Strouhal numbers by the interaction length scale and freestream velocity, $\mathrm{St} = fL/U_\infty$. The interaction length scale is chosen as the first streamwise skin friction zero-crossing to the inviscid shock impingement location, or R3 to I in Table 4.

Figure 28 shows the upstream and downstream probe PSD plots with a representative point from the intermittent reflecting shock foot location, R2. All curves show a broadband peak at higher Strouhal numbers near $\mathrm{St} \approx 1-3$. This broadband frequency content comes from the turbulent boundary layer upstream of the interaction region and is expected for an incident SWBLI such as this case. Looking first at the R2 curve, the power in the lower Strouhal number range is clearly higher than either upstream or downstream of the flow. The broadband higher Strouhal number peak for the R2 curve is much diminished, roughly halved, compared to the upstream or downstream PSD curves. There is a peak in the Strouhal number near $\mathrm{St} \approx 0.09$ for the R2 curve. The data collection period was determined by using the dimensional frequency associated with this peak. The dimensional frequency is roughly 2441 Hz. With the time step of $\Delta t = 1 \times 10^{-7}$ s, 102 cycles of this peak were collected in the time history subdomains. Additional peaks in the spectra are seen at $\mathrm{St} \approx 0.19, 0.39$, and 0.5. These intermediate Strouhal number peaks are also visible in the upstream and downstream curves. The interaction region seems to increase the power in these frequencies as the downstream curves have much higher peaks at those Strouhal numbers. The downstream PSD does retain a slight increase at the lowest dominant frequency peak $\mathrm{St} \approx 0.09$, and the broadband is shifted to slightly lower Strouhal numbers compared to the

upstream.

The characteristic recycling frequency as determined by the recycling/rescaling length over the freestream velocity is roughly 2940 Hz. This frequency corresponds to a Strouhal number of St $\approx$ 0.11. It does not appear the intermediate Strouhal number peaks are associated with the recycling/rescaling method. Morgan et al. [35] investigated the low-frequency behavior of various recycling/rescaling implementations. Some recycling/rescaling implementations were found to introduce unwanted low-frequency energy. The methods which Morgan et al. describe as most similar to the random spanwise shifting used by VULCAN-CFD [31] did not introduce nonphysical low-frequency content to energy spectra.

Figure 29 shows the R2 curve again from the intermittent reflected shock foot location, but now the accompanying curves represent points under the mean separation bubbles associated with the reflected shock foot and the inviscid shock impingement locations. The minimum C_{fx} and inviscid shock impingement PSD are similar to each other with broadband peak being St $\approx$ 1 for both curves. Both also have elevated low Strouhal values which suggests the reflected shock foot low-frequency content is still present in the interaction region even with the two mean separation bubbles, but is diminished by the downstream station. Further analysis might be able to help understand driving and driven mechanisms in this case. The upstream and downstream influences on SBWLI unsteadiness has been a research focus in the community for some time [6].

Figure 30 shows the spectra at the probe locations near the reflected shock foot location. Locations R1 and R2 were selected after other analysis provided the initial pressure rise and $C_{fx} = 0$ axial locations. The R1 curve does not show the large peak at St $\approx$ 0.09 that is seen in the other two curves. One might expect the mean pressure rise location to also move with the same frequency content as the separated region directly downstream of it, but the R1 curve is more similar to the upstream station. There is a rise in the PSD at the low-frequency tail of the R1 curve that is not seen in any other PSD taken. There could be an even lower frequency spike for this location, but longer computational runs would be required to determine this. The R3 curve strongly mirrors the R2 curve with a slight shifting of the broadband portion of the PSD to lower values. The $C_{fx} = 0$ point has the low-frequency peak associated with the reflected shock unsteadiness, but the pressure rise location does not. Figure 31 stacks PSD by vertically shifting each curve by 0.5. This allows some of the broadband shifting to be visualized more clearly. Without the overlapping curves it is also easier to spot the intermediate Strouhal peaks across the PSD curves.

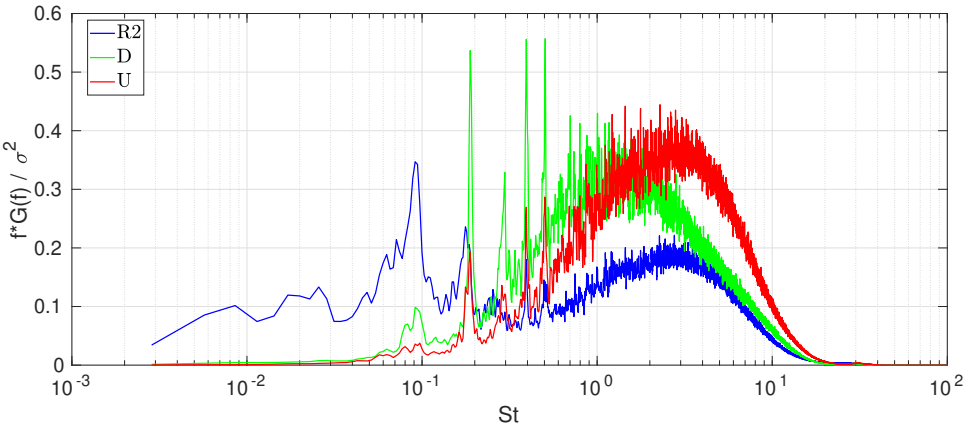

Fig. 28 PSD at reflected shock foot, downstream, and upstream locations.

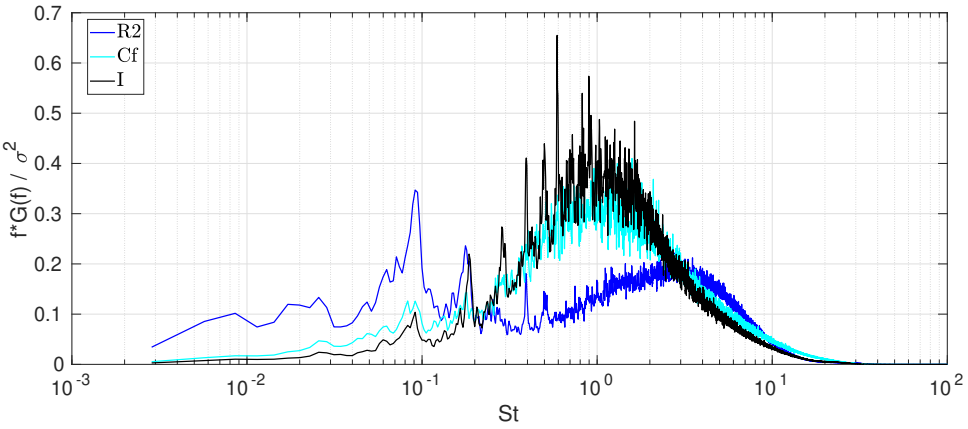

Fig. 29 PSD at reflected shock foot, minimum C_{fx}, and inviscid shock impingement locations.

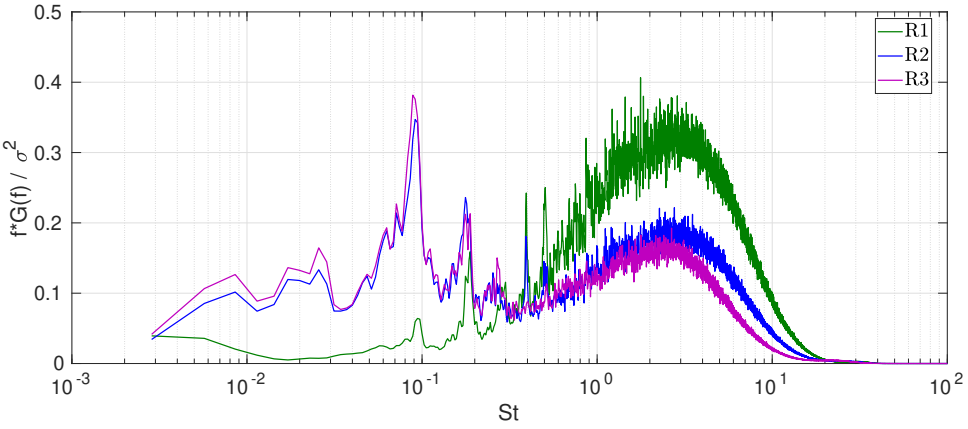

Fig. 30 PSD near reflected shock foot locations.

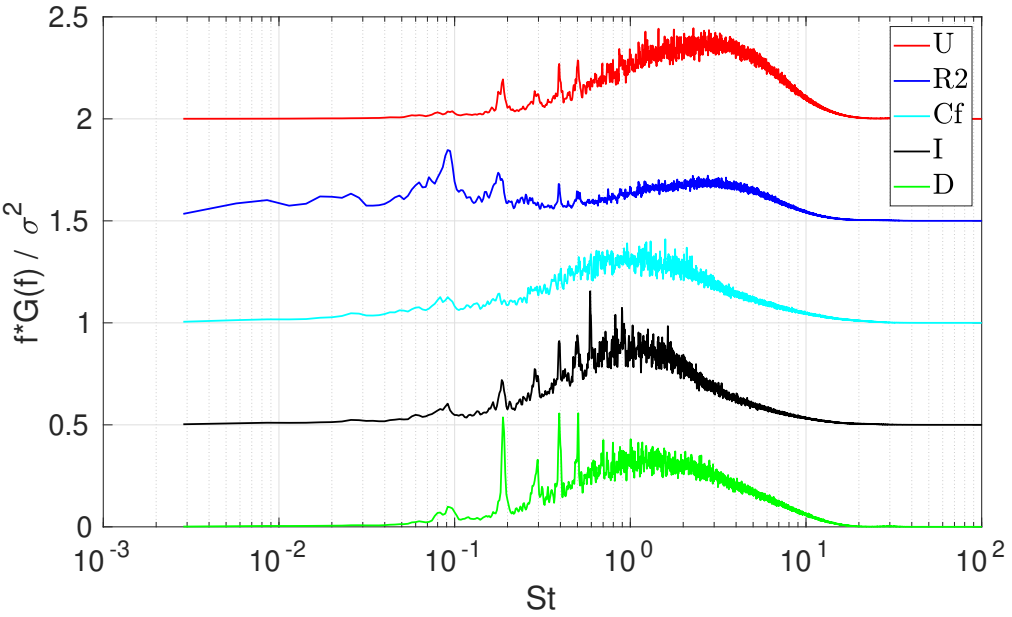

Fig. 31 Weighted PSD.

IV. Conclusions and Future Work

An implicit large-eddy simulation was completed and compared to the Turbulent Computational Fluid Dynamics Validation Experiment from NASA Glenn Research Center. The freestream Mach number was 2.5 in the axisymmetric configuration. The ILES simulation spanned a 25-degree sector of the wind tunnel wall and included 2 billion computational grid points. The grid resolution approached DNS quality. VULCAN-CFD was used with fourth-order low-dissipation methods enabled and recycling/rescaling to produce a scale-resolved turbulent boundary layer. A precursor RANS simulation of the entire wind tunnel was completed to generate boundary conditions. The boundary layer achieved was evaluated against the experimental data. The time averaging and time history collection of data were described and some images showing qualitative overview of the simulation were shown. Wall pressure and streamwise skin friction coefficient were evaluated to comment on the SWBLI induced separation. Instantaneous contours of C_{fx} showed intermittent separation. Time averaged contours of C_{fx} showed a roughly uniform azimuthal separation near the reflected shock foot, but distinct cells of separation near the inviscid shock impingement location of the incident shock. In the azimuthal average of the time average of C_{fx}, two distinct separation bubbles were present. As the focus of the case represents a striving towards an axisymmetric case with minimized natural three-dimensionality, this result reinforces the caution one must have in making simplifying assumptions, nominally axisymmetric, to complex fluid phenomenon.

Contours of primitive variables and Reynolds stress components were presented to overview relevant flow phenomenon. Some instantaneous contours were used to illustrate the scale-resolved turbulence in the computation. Computational results were then compared to PIV, Pitot probe, wall static pressure taps, and hot-wire survey data. PIV data at the highest Reynolds number of $\mathrm{Re}_D = 4E6$ collapsed with the ILES data at $\mathrm{Re}_D = 1E6$. The cause for the $\mathrm{Re}_D = 1E6$ and $\mathrm{Re}_D = 2E6$ PIV data not comparing as well to the ILES data is not clear. At higher Mach number and Reynolds number combinations not yet simulated, the PIV data collapsed much better using the same scaling, see Ref. [16]. Future ILES calculations at those conditions with better data agreement may clarify the disagreement. The Pitot and hot-wire data at $\mathrm{Re}_D = 4E6$ also compare well with the ILES. Hot-wire data provided mass flux turbulent intensities to compare to the ILES. Future work could include additional analysis of the unsteady aspects of the flow beyond those with direct experimental comparisons available. Power spectral densities of pressure at several locations of interest allowed some temporal analysis of the data. The SWBLI in the ILES does demonstrate the low-frequency behavior near the reflecting shock foot as expected. Additional work could be completed to investigate the effect on the low-frequency dynamics of the flow separating intermittently and having two distinct separation bubbles in the time average as opposed to one. Further analysis of this dataset as well as the completion of additional ILES at higher Mach

number and Reynolds number could prove useful to the turbulence modeling community as another point of comparison between a high-quality experimental dataset with multiple complementary methods and high-resolution computational efforts.

Acknowledgments

The first author was supported by an NDSEG Fellowship. The authors would like to thank Dr. Robert Baurle for his time and the many helpful discussions about VULCAN-CFD which made this research possible. The authors would also like to thank Dr. Heath Reising and Dr. Dave Davis from NASA Glenn Research Center for their collaboration on the experimental side. This work is also supported in part by a grant of computer time from the DoD High Performance Computing Modernization Program at the ERDC DoD Supercomputing Resource Center.

References

[1] Settles, G. S., and Dodson, L. J., "Supersonic and hypersonic shock/boundary-layer interaction database," *AIAA Journal*, Vol. 32, No. 7, 1994, pp. 1377–1383. https://doi.org/10.2514/3.12205.

[2] DeBonis, J. R., Oberkampf, W. L., Wolf, R. T., Orkwis, P. D., Turner, M. G., Babinsky, H., and Benek, J. A., "Assessment of Computational Fluid Dynamics and Experimental Data for Shock Boundary-Layer Interactions," *AIAA Journal*, Vol. 50, No. 4, 2012, pp. 891–903. https://doi.org/10.2514/1.J051341.

[3] Gaitonde, D. V., and Adler, M. C., "Dynamics of Three-Dimensional Shock-Wave/Boundary-Layer Interactions," *Annual Review of Fluid Mechanics*, Vol. 55, No. 1, 2023, pp. 291–321. https://doi.org/10.1146/annurev-fluid-120720-022542.

[4] Poggie, J., and Porter, K. M., "Flow structure and unsteadiness in a highly confined shock-wave–boundary-layer interaction," *Phys. Rev. Fluids*, Vol. 4, 2019, p. 024602. https://doi.org/10.1103/PhysRevFluids.4.024602.

[5] Vyas, M., "Three-dimensional Effects on Unsteady Dynamics and Turbulent Transport Mechanisms of an Impinging Shock Wave/Boundary-layer Interaction," Ph.D. thesis, The Ohio State University, 2021.

[6] Clemens, N. T., and Narayanaswamy, V., "Low-Frequency Unsteadiness of Shock Wave/Turbulent Boundary Layer Interactions," *Annual Review of Fluid Mechanics*, Vol. 46, No. 1, 2014, pp. 469–492. https://doi.org/10.1146/annurev-fluid-010313-141346.

[7] Mosele, J.-P. G., Gross, A., Slater, J., Davis, D., and Vyas, M. A., "Axisymmetric and Asymmetric Turbulent Shockwave Boundary Layer Interaction at Mach 2.5," AIAA Paper 2021-2763, July 2024. https://doi.org/10.2514/6.2021-2763.

[8] Mosele, J.-P., Gross, A., and Slater, J., "Numerical Investigation of Asymmetric Mach 2.5 Turbulent Shock Wave Boundary Layer Interaction," *Aerospace*, Vol. 10, No. 5, 2023. 417, https://doi.org/10.3390/aerospace10050417.

[9] Mosele, J.-P., Gross, A., and Slater, J., "Numerical Investigation of Mach 2.5 Axisymmetric Turbulent Shock Wave Boundary Layer Interactions," *Aerospace*, Vol. 10, No. 2, 2023. 159, https://doi.org/10.3390/aerospace10020159.

[10] Friedlander, D. J., Georgiadis, N. J., Howerton, L. W., and Reising, H. H., "Numerical Simulations of an Axisymmetric Shock-Wave/Boundary-Layer Interaction," AIAA Paper 2025-2065, January 2025. https://doi.org/10.2514/6.2025-2065.

[11] Davis, D. O., "CFD Validation Experiment of a Mach 2.5 Axisymmetric Shock-Wave/Boundary-Layer Interaction," *Proceedings of the ASME/JSME/KSME 2015 Joint Fluids Engineering Conference*, Vol. Volume 1: Symposia, 2015. V001T06A001, https://doi.org/10.1115/AJKFluids2015-6342.

[12] Sasson, J., Davis, D. O., Barnhart, P., and Reising, H. H., "Summary of a Mach 2.5 Shock Wave Turbulent Boundary Layer Interaction Experiment in a Circular Test Section," AIAA Paper 2023-0442, January 2023. https://doi.org/10.2514/6.2023-0442.

[13] Sasson, J., "Conical Shock Wave Turbulent Boundary Layer Interactions in a Circular Test Section at Mach 2.5," Ph.D. thesis, Case Western Reserve University, 2022.

[14] Reising, H. H., and Davis, D. O., "PIV Measurements of Shock-Wave/Boundary-Layer Interactions at Mach 2.5 in a Circular Test Section," AIAA Paper 2024-2554, January 2024. https://doi.org/10.2514/6.2024-2554.

[15] Reising, H. H., Sasson, J., Davis, D. O., Friedlander, D., and Howerton, L. W., "Cross-Measurement Comparisons for a CFD Validation Dataset on Mach 2.5 Axisymmetric Turbulent Shock-Wave/Boundary-Layer Interactions," AIAA Paper 2025-0474, January 2025. https://doi.org/10.2514/6.2025-0474.

[16] Reising, H. H., "Turbulent Shock-Wave/Boundary-Layer Interactions Without Sidewall Effects at Mach 2.5, 3.0, and 3.5 — PIV Measurements From 2025 Test Entry," NASA/TM-2025-0008885, September 2025.

[17] Cadence Design Systems Inc., "Fidelity Pointwise User Manual," https://www.cadence.com/doc/user-manual/, Accessed 2025.

[18] Tecplot, "Tecplot 360 Version 2021r2," https://www.tecplot.com/products/tecplot-360/, Accessed 2025.

[19] The MathWorks Inc., "MATLAB version: 9.13.0 (R2022b)," https://www.mathworks.com, Accessed 2025.

[20] Baurle, R. A., White, J. A., O'Connell, M. D., Drozda, T. G., and Norris, A. T., "VULCAN-CFD User Manual: Ver. 7.2.0," NASA/TM-2022-0008781, November 2022.

[21] Baurle, R. A., White, J. A., Drozda, T. G., and Norris, A. T., "VULCAN-CFD Theory Manual: Ver. 7.2.0," NASA/TM-2022-0008776, November 2022.

[22] Spalart, P. R., and Allmaras, S. R., "A One-Equation Turbulence Model for Aerodynamic Flows," *Recherche Aerospatiale*, Vol. 1, 1994, pp. 5–21.

[23] Edwards, J. R., "A Low-Diffusion Flux-Splitting Scheme for Navier-Stokes Calculations," *Computers & Fluids*, Vol. 26, No. 6, 1997, pp. 635–659.

[24] Poggie, J., Bisek, N. J., and Gosse, R., "Resolution effects in compressible, turbulent boundary layer simulations," *Computers & Fluids*, Vol. 120, 2015, pp. 57–69.

[25] Georgiadis, N. J., Rizzetta, D. P., and Fureby, C., "Large-Eddy Simulation: Current Capabilities, Recommended Practices, and Future Research," *AIAA Journal*, Vol. 48, No. 8, 2010, pp. 1772–1784. https://doi.org/10.2514/1.J050232.

[26] White, J., Baurle, R., Fisher, T., Quinlan, J., and Black, W., "Low-Dissipation Advection Schemes Designed for Large Eddy Simulations of Hypersonic Propulsion Systems," AIAA Paper 2012-4263, August 2012.

[27] Baurle, R. A., "Hybrid Reynolds-Averaged / Large Eddy Simulation of a Cavity Flameholder; Assessment of Modeling Sensitivities," AIAA Paper 2015-0637, January 2015.

[28] Baurle, R. A., "Hybrid Reynolds-Averaged/Large-Eddy Simulation of a Scramjet Cavity Flameholder," *AIAA Journal*, Vol. 55, No. 2, 2017, pp. 544–560. https://doi.org/10.2514/1.J055339.

[29] Suresh, A., and Huynh, H., "Numerical experiments on a new class of nonoscillatory schemes," AIAA Paper 1992-0421, 1992.

[30] Litton, D., Edwards, J., and White, J., "Algorithmic Enhancements to the VULCAN Navier-Stokes Solver," AIAA Paper 2003-3979, 2003.

[31] Boles, J., Choi, J.-I., Edwards, J., and Baurle, R., "Multi-Wall Recycling / Rescaling Method for Inflow Turbulence Generation," AIAA Paper 2010-1099, 2010.

[32] Bernardini, M., Della Posta, G., Salvadore, F., and Martelli, E., "Unsteadiness characterisation of shock wave/turbulent boundary-layer interaction at moderate Reynolds number," *Journal of Fluid Mechanics*, Vol. 954, 2023, p. A43. https://doi.org/10.1017/jfm.2022.1038.

[33] Dupont, P., Haddad, C., and Debiève, J. F., "Space and time organization in a shock-induced separated boundary layer," *Journal of Fluid Mechanics*, Vol. 559, 2006, p. 255–277. https://doi.org/10.1017/S0022112006000267.

[34] Smits, A. J., McKeon, B. J., and Marusic, I., "High–Reynolds Number Wall Turbulence," *Annual Review of Fluid Mechanics*, Vol. 43, 2011, pp. 353–375.

[35] Morgan, B., Larsson, J., Kawai, S., and Lele, S. K., "Improving Low-Frequency Characteristics of Recycling/Rescaling Inflow Turbulence Generation," *AIAA Journal*, Vol. 49, No. 3, 2011, pp. 582–597. https://doi.org/10.2514/1.J050705.